NASA TECHNICAL NOTE
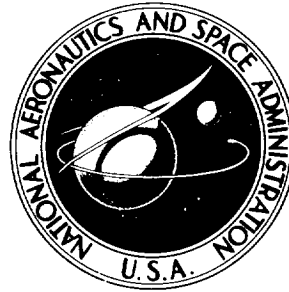
NASA TN D-8150

PERFORMANCE OF LI-1542 REUSABLE SURFACE INSULATION SYSTEM IN A HYPERSONIC STREAM

L. Roane Hunt, John L. Shideler,
and Irving Weinstein

Langley Research Center
Hampton, Va. 23665

NATIONAL AERONAUTICS AND SPACE ADMINISTRATION • WASHINGTON, D. C. • MARCH 1976

1. Report No. NASA TN D-8150	2. Government Accession No.	3. Recipient's Catalog No.
4. Title and Subtitle PERFORMANCE OF LI-1542 REUSABLE SURFACE INSULATION SYSTEM IN A HYPERSONIC STREAM		5. Report Date March 1976
		6. Performing Organization Code
7. Author(s) L. Roane Hunt, John L. Shideler, and Irving Weinstein		8. Performing Organization Report No. L-10551
		10. Work Unit No. 506-17-22-01
9. Performing Organization Name and Address NASA Langley Research Center Hampton, Va. 23665		11. Contract or Grant No.
		13. Type of Report and Period Covered Technical Note
12. Sponsoring Agency Name and Address National Aeronautics and Space Administration Washington, D.C. 20546		14. Sponsoring Agency Code

15. Supplementary Notes

16. Abstract

   The thermal and structural performance of a large panel of LI-1542 reusable surface insulation (RSI) tiles was determined by a series of cyclic heating tests using radiant lamps and aerothermal tests in the Langley 8-foot high-temperature structures tunnel. The test panel was designed to represent part of the surface structure on a space shuttle orbiter fuselage along a 1250 K isotherm. Aerothermal tests were conducted at a free-stream Mach number of 6.6, a total temperature of 1820 K, Reynolds numbers of 2×10^6 and 5×10^6 per meter, and dynamic pressures of 26 and 65 kPa. The RSI tiles demonstrated good thermal protection and good structural integrity. The thermal response of the RSI tile was predictable and repetitive. During aerothermal tests, high temperatures were caused by misalinement in tile height, offset in tile longitudinal alinement, and leakage around thermal seals when differential pressure across the panel existed. The damage tolerance of LI-1542 RSI appeared to be very high. The tile coating crazed early in the test program, but this did not affect the tile integrity. Considerable erosion of the tile edges occurred at forward-facing steps and at the ends of longitudinal gaps because of the combined effects of particle impacts and flow shear.

17. Key Words (Suggested by Author(s)) Hypersonic Thermal protection Surface insulation	18. Distribution Statement Unclassified – Unlimited Subject Category 18
19. Security Classif. (of this report) Unclassified	20. Security Classif. (of this page) Unclassified	21. No. of Pages 69	22. Price* $4.25

PERFORMANCE OF LI-1542 REUSABLE SURFACE INSULATION
SYSTEM IN A HYPERSONIC STREAM

L. Roane Hunt, John L. Shideler, and Irving Weinstein
Langley Research Center

SUMMARY

The thermal and structural performance of a large panel of LI-1542 reusable surface insulation (RSI) tiles was determined by a series of cyclic heating tests using radiant lamps and aerothermal tests in the Langley 8-foot high-temperature structures tunnel. The test panel was designed to represent part of the surface structure on a space shuttle orbiter fuselage along a 1250 K isotherm. Aerothermal tests were conducted at a free-stream Mach number of 6.6, a total temperature of 1820 K, Reynolds numbers of 2×10^6 and 5×10^6 per meter, and dynamic pressures of 26 and 65 kPa. The RSI tiles demonstrated good thermal protection and good structural integrity. The thermal response of the RSI tile was predictable and repetitive. During aerothermal tests, high temperatures were caused by misalinement in tile height, offset in tile longitudinal alinement, and leakage around thermal seals when differential pressure across the panel existed. The damage tolerance of LI-1542 RSI appeared to be very high. The tile coating crazed early in the test program, but this did not affect the tile integrity. Considerable erosion of the tile edges occurred at forward-facing steps and at the ends of longitudinal gaps because of combined effects of particle impacts and flow shear.

INTRODUCTION

Thermal protection systems (TPS) of current and future space transports are a major area of technological development which requires thorough experimental evaluation prior to preflight verification. (See refs. 1 and 2.) In support of this requirement, the Langley Research Center initiated an extensive testing program for assessing the thermal and structural performance of various candidate systems in a realistic aerothermal environment. (See refs. 3 and 4.) For this program, several full-scale TPS panels were designed by use of different structural concepts. One of the panels includes reusable surface insulation (RSI) similar to that chosen for the space shuttle. This panel was subjected to a series of thermal-structural cyclic tests, and the results are reported herein. These test results, in preliminary form, were presented in reference 5.

The test panel consisted of RSI tiles (designated LI-1542) bonded to subpanels that were supported by the primary structure. It was designed and fabricated by Lockheed Missiles and Space Company (ref. 6) to represent part of the surface structure on a shuttle orbiter fuselage along a 1250 K isotherm. The test panel was subjected to 23 thermal tests, 6 of which combined radiant and aerodynamic heating test segments to represent an entry temperature history. Also, 6 of the thermal tests were made by use of only aerodynamic heating to determine the thermal response of the panel to this type of heating without the influence of radiant heat exposure. The remaining 11 thermal tests used only the radiant heating at atmospheric pressure to demonstrate reuse capability. All tests were conducted in the Langley 8-foot high-temperature structures tunnel. For the aerodynamic heating tests, the free-stream Mach number was 6.6, the total temperature was 1820 K, the Reynolds numbers were 2×10^6 and 5×10^6 per meter, and the dynamic pressures were 26 and 65 kPa.

Thermal and stress analyses of the RSI are included herein with details presented in the appendixes. Comparison of the thermal analysis with experimental results helped to confirm the validity of the analytical model. The stress analysis was used to determine the effect of thermal stress on the allowable size of RSI tiles.

SYMBOLS

C_p specific heat at constant pressure, J/kg-K

E modulus of elasticity, Pa

G shear modulus, Pa

k thermal conductivity, W/m-K

M Mach number

p pressure, Pa

q dynamic pressure, Pa

R_L unit Reynolds number, m^{-1}

T temperature, K

t time, s

2

x,y,z	panel (fig. 7) and tile (fig. 33) coordinates, m
α	angle of attack, deg; and coefficient of thermal expansion, K^{-1}
Δp	differential pressure load on test panel, Pa
ϵ	emissivity
σ	tensile or compressive stress, Pa
τ	shear stress, Pa

Subscripts:

c	coating
l	local flow
o	initial
t	total
ult	ultimate stress
x	x-direction (tile inplane)
z	z-direction (tile crossplane)
∞	free-stream flow

APPARATUS AND TESTS

Panel Description

The TPS panel used in the present test program was designed to meet the mission requirements given in reference 6. As shown in figure 1, it consists of an array of 24 RSI tiles bonded to a support structure. Overall dimensions are 108 by 152 by 12.7 cm. Each RSI tile (designated LI-1542) consists of rigidized, silica-fiber insulation (designated LI-1500) and a borosilicate coating (designated LI-0042) containing a silicon carbide

emittance agent. All tiles were impregnated with a hydrophobic agent. The eight center tiles are 29.11 cm square and 3.18 cm thick including the coating thickness of 0.25 mm. These center tiles are bonded to two beryllium subpanels which are offset by 2.5 cm to limit the length of longitudinal gaps between tiles to 58 cm. Sixteen peripheral tiles are sized to close out the panel test area. The peripheral tiles and the subpanels are sup-ported by a titanium frame. Average unit mass of the RSI and subpanels combined is 16.43 kg/m^2, as indicated in table I where the unit masses of the TPS components are given. Insulation and coating densities are 240 and 1670 kg/m^3, respectively.

The stringer-stiffened beryllium subpanel, shown in figure 2, is the basic structural unit of the test panel. Each subpanel supports four RSI tiles, is 55.9 cm square, and is fabricated from 1.0-mm sheets. The subpanels were attached along their periphery to the support frame with 12 rivets each.

The titanium frame, shown in figure 3, represents the primary structure which would support individual subpanels in a flight design. The top of the frame is covered by 0.64-cm-thick titanium plates around the area reserved for the two subpanels. The plates are held off the frame by spacers, and the peripheral tiles are bonded directly to these plates. Titanium channels, shown in the bottom view, have a web height of 6.0 cm, flange width of 3.18 cm, and a thickness of 0.127 cm. An aluminum plate (0.8 mm thick) was attached directly to the bottom of the frame to absorb the internal radiation of the test panel.

The tile installation procedure is illustrated in figure 4, which shows the titanium frame with subpanels attached. The procedure began by covering the entire upper sur-face of this assembly with a 0.23-cm-thick layer of silicone rubber (RTV 560). This layer served as a strain isolator for the RSI tiles. Before the rubber hardened, strips were placed in the rubber to outline the tile positions. When these strips were removed, a groove pattern remained that isolated the tiles as shown in figure 4(a). The tiles and a thermal seal between tiles were then bonded in place with a very thin layer of RTV 560. The tile placement relative to the groove pattern is illustrated in figure 4(b).

The structural configuration of the test panel is further illustrated in the cross sec-tions shown in figure 5. These views of the tile gaps and panel joints are typical of those throughout the panel. Figure 5(a) shows a typical border joint between the peripheral tile support and the subpanels. Figure 5(b) shows a typical interior gap above a continuous support. Figure 5(c) shows the spanwise joint between subpanels which is a true repre-sentation of a panel joint of the flight design. The joints were located directly above the back-to-back channels of the frame. The gaps between tiles are 1.0 mm wide, and the exposed sides of the tiles are coated. All the tile edges are undercut from the bottom surface by 1.27 cm to a height of one-half the tile thickness (1.59 cm) to receive the ther-mal seal. Thus, the undercut surfaces are not coated. However, the top surface of the

4

thermal seal is coated with the LI-0042 material. The seal is designed to prevent hot gases in the tile gap from penetrating to the bond and substructure. It is made of a soft fibrous-silica material whose density is 96 kg/m^3.

Panel Holder

TPS panel tests were performed with the panel holder shown in figure 6. The panel holder is a rectangular slab 141 by 300 cm with a 20° bevel at the leading edge. A cutout, that can accommodate test panels up to 108 by 152 cm, is located 102 cm from the leading edge. Tests are made by use of the panel holder pitched at angles to the test stream varying from 0° to 15°. The panel holder has boundary-layer flow trips and aerodynamic fences to provide uniform aerodynamic pressure and heat-transfer loading to the test panel surface. A single row of spheres, spaced across the panel holder width 12.7 cm from the sharp leading edge, trips the boundary layer to provide turbulent flow over the test surface. Aerodynamic fences on the side edges of the panel holder extend 7.6 cm above the test surface to channel the flow over the test surface when the holder is pitched relative to the stream. The fences extend 25 cm below the bottom of the holder to prevent vortical flow spilling on to the test surface from the bottom surface at angles of attack near zero. The maximum surface pressure and cold-wall heat-transfer rate possible for the available test conditions are 15 kPa and 250 kW/m^2, respectively. The flow calibration of the panel holder is described in reference 7.

The present test panel was installed in the cutout of the panel holder so that the test surfaces of the panel and panel holder were flush. The panels are supported from the bottom by longitudinal structural beams attached to the sidewalls of the cutout. The bottom of the cutout is covered by an access door that provides a usable space 25 cm deep between the door and the test surface for the panel and instrumentation. The space below the test panel can be vented to the low base pressure of the holder, or it can be pressurized mechanically to vary the differential pressure loading across the panel depth. Normally, when this space is sealed, the pressure beneath the panel will equalize with that above the panel because of leakage at the panel edges. Additional information on the panel-holder pressure-control system may be found in reference 8.

Panel Instrumentation

The test panel is instrumented with 65 thermocouples (TC): 45 in the RSI tiles and 20 on the subpanel and support frame. The locations of these thermocouples are indicated in figure 7 by symbols. Figure 7(a) shows thermocouple locations for the subpanel tiles identified by Roman numerals. Figure 7(b) shows thermocouple locations on the subpanels and support frame. The Cartesian coordinates and the alphanumeric system shown in figures 7(a) and 7(b) will be useful in discussing results subsequently.

The thermocouples located in the RSI tiles were prescribed to be at the top surface and at depths of 0.51, 1.27, and 2.29 cm from the top surface. They were embedded in plugs of insulation which were then inserted into holes in the tile before the tile was coated. To verify the location of the thermocouples, X-ray photographs were taken of a typical thermocouple plug after the tests, and two views are presented as figure 8. The thermocouples seem to have been located properly; however, the surface thermocouple appears to be at a depth of about 1 mm. The bead extends up to the coating, but the lead wires are parallel to and below the top surface. The effective depth of this thermocouple was assumed to be the depth of the lead wire.

The surface temperature distribution was also determined by using a scanning infrared radiometer. Thermal radiation from the panel surface was monitored by a photovoltaic indium-antimonide detector which mechanically scanned the surface with a nominal spatial resolution of 1.3-cm diameter. The radiometer viewed a surface area of about 70 by 90 cm or from rows 1 to 5 and from rows B to H. (See fig. 7(a).) This system was sensitive to a temperature range from 650 K to 1400 K. Further information about the radiometer is presented in references 3 and 8.

Facility

The tests were conducted in the Langley 8-foot high-temperature structures tunnel (HTST) shown schematically in figure 9. This facility is a hypersonic blowdown wind tunnel that uses the combustion products of methane and air as the test medium and operates at a nominal Mach number of 7, at total pressures between 3.4 and 24.1 MPa, and at nominal total temperatures between 1400 K and 2000 K. Corresponding free-stream unit Reynolds numbers are between 1×10^6 and 10×10^6 per meter. These conditions simulate the aerothermal flight environment at Mach 7 in the altitude range between 25 and 40 km. As indicated in figure 9, the panel holder is retained in the pod below the test chamber during facility startup and shutdown so that the panel is exposed only to the desired stream conditions.

Although the facility provides aerodynamic exposure times of up to 120 seconds, thermal exposure times can be extended indefinitely by means of a pair of retractable quartz-lamp radiant heaters located in the pod. These heaters and the entire test surface of the panel holder are covered by a pair of acoustic baffles which protect the panel from potentially damaging acoustic disturbance and buffeting generated during facility startup and shutdown. Sketches of the radiant heaters and acoustic baffles are shown in figure 10. The sketches in figure 11 show the panel holder covered by the heaters during pretest and posttest conditions and also show the panel holder in test position with heaters retracted. Additional information pertaining to this equipment and the test facility may be found in references 7 and 8.

6

Test Procedure

The RSI test panel was repeatedly exposed to the three surface temperature histories identified as test modes in figure 12. These test modes were previously used in the evaluation of a metallic TPS reported in reference 3. For test mode I (fig. 12(a)), the thermal load is provided by radiant heaters only. It is characterized by a linear heating period at 2 K/s to a surface temperature of about 1100 K, a constant-temperature period of nominally 1000 seconds, and a controlled cooldown period at 2 K/s until the natural cooling process dominates. For test mode II (fig. 12(b)), the thermal load is aerodynamically induced by the tunnel stream. In this test, the panel is at ambient temperature upon insertion into the stream. Its surface temperature then rises very rapidly, approaches a steady-state level within approximately 30 seconds, and decreases naturally after withdrawal from the stream. This type of test provides the opportunity to observe panel thermal response to aerodynamic heating. Test mode III (fig. 12(c)) is a combination of modes I and II in which the panel is radiantly preheated at a constant temperature for approximately 700 seconds and then is aerodynamically heated for approximately 40 seconds. In this test, tunnel stream conditions and angle of attack are selected to sustain the preheated surface temperature. Thus, in this type of test, an entry thermal history which includes a short exposure to the aerodynamic heating and pressure loads can be imposed upon the test panel.

Tests

The test panel was exposed to a total of 23 thermal cycles: 11 in mode I, 6 in mode II, and 6 in mode III. The sequences of tests and test conditions are listed in table II. After an initial mode I test was conducted, five tests were conducted in mode II; however, tests 2 and 4 were abbreviated by tunnel flow breakdown and combustor flameout, respectively. In subsequent tests, modes I and III were interspersed; and many of the mode I tests, whose constant-temperature period was about 700 seconds, were radiant heating portions of mode III tests that ended by natural cooling, of the panel because the tunnel did not operate properly. In all but one of the mode III tests, the panel was exposed to aerodynamic heating at $\alpha = 15^\circ$; in test 11, the panel was at $\alpha = 0^\circ$. Except for tests 22 and 23, the panel-holder cavity space below the panel was vented to a low pressure at the base of the panel holder, and the differential pressure (Δp) varied from 4.94 to 8.41 kPa for those tests at $\alpha = 15^\circ$. For tests 22 and 23, this space was very nearly sealed, and the resulting Δp was 0.11 kPa. Just prior to test 23, two tiles were soaked with water and then exposed to the rapid heat-up of the mode II test.

Flow conditions for the aerodynamic heating tests (modes II and III) are given in table III. Free-stream total temperature, unit Reynolds number, dynamic pressure, Mach number, and static pressure are given for each test. Local dynamic pressure,

Mach number, and static pressure are also given. The local flow conditions differ from the free-stream conditions when the panel holder is pitched at α greater than zero.

RESULTS AND DISCUSSION

Thermal Response

RSI system.- To evaluate the thermal performance of the RSI concept, the thermal histories of the various test modes were compared with predictions by use of the thermal analysis described in appendix A. This analysis used a one-dimensional model through the tile and subpanel between supports. The analysis of experimental results presented in appendix A indicates that the thermal properties as presented in table IV (see refs. 6 and 9) are adequate for predicting thermal response of the RSI interior for the long-duration radiant heating of the mode I test. Also, an accurate value of surface emissivity of the RSI coating was necessary to predict thermal response of RSI when exposed to the aerodynamic heating of the mode II tests. Surface emissivities from two measurement techniques (the reflectance technique of ref. 9 and the self-emission technique of ref. 10) were available. The surface emissivity of reference 10 was preferred to that of reference 9 in the prediction of thermal response of the present tests.

The temperature histories at various depths in the insulation and of the subpanel for a typical mode III test, which represents a shuttle entry, are presented in figure 13(a). The panel was radiantly heated for 1140 seconds and aerodynamically heated for 40 seconds followed by natural cool-down. The temperatures from thermocouples (indicated by the solid curves) agreed with the predicated temperatures (indicated by the dashed curves). The aerodynamic heating part of the test is presented in figure 13(b). In this figure the test data shown at $z = 0$ (solid symbols) were from the infrared radiometer and are in excellent agreement with predicted results. As indicated in figures 13(a) and 13(b), the thermal response of the panel to both radiant and aerodynamic heating was predictable, by using published thermal properties and the simple analytical model. The RSI provided good thermal protection for heat exposures up to 2210 seconds (see table II) since the beryllium subpanel temperature remained well below the design limit of 590 K (ref. 6). However, the thermal protection of the subpanel design during the aerodynamic exposure was not adequate at the joints as discussed in a subsequent section.

The thermal protection capability of the RSI over many cycles is demonstrated in figure 14 where the first 1100 seconds of the RSI temperature histories of tests 10 and 22 are compared. Test 10 is one of the first mode III tests, and test 22 is the last. Although the temperatures of test 10 were slightly higher than those of test 22, the curves for the two tests are very similar. The repeatability of thermal response shown in figure 14

8

indicates that the thermal performance of the RSI did not deteriorate during the numerous thermal cycles imposed on the panel.

RSI tile gaps.- In the present tests, temperatures within tile gaps were in many cases greater than those on the tile upper surface. These excessive temperatures were observed by optical photography, infrared radiometer, and thermocouple instrumentation. They were caused by small variations in tile height that produced forward-facing steps, flow stagnation at the ends of longitudinal gaps where tiles were offset, and penetration of the gas past the thermal seals.

A photograph of the visible glow of the hot RSI surface produced by aerodynamic heating during test 10 is shown in figure 15(a). The tile surfaces are glowing at a temperature of about 1210 K. The glow along tile edges is significantly brighter than that of the surface, to the extent that the tile arrangement of the panel is outlined, and indicates that temperatures there are considerably higher than those on the tile surface. Moreover, even hotter spots caused by stagnating flow at the ends of longitudinal gaps are clearly defined at the "tee" intersections of gaps along rows A, E, and I with gaps along rows 1, 3, and 5. The glow in the longitudinal gaps at the subpanel border joints (rows 1 and 5) is much brighter than that of the interior gap along row 3. This excessive heating was subsequently attributed to flow leakage past the border joint seals (fig. 5(a)) and discussed in a later section. The glow in the lateral gap along row I is brighter than in other lateral gaps and resulted from exposure of the lower emissivity insulation material caused by erosion of the coating.

The surface isotherm plot for test 10 presented in figure 15(b), which was obtained from radiometer data, shows distinct features of the temperature pattern, especially at the gaps. For example, the hot spots at the end of longitudinal gaps at locations E1, E3, and E5 (intersection of rows 1, 3, and 5 with row E) are clearly evident with isotherms as high as 1240 K. Cool spots are also apparent along lateral gaps at locations C4 and E2 with isotherms as low as 1180 K. These cool spots may have resulted from flow ejecting from the gaps behind rearward-facing steps of about 0.2 mm at those locations.

The temperatures deep in the gaps were measured by the thermocouples located just under the lip where the tiles were undercut. Typical temperature histories of gaps around tile I (fig. 7(a)) for the radiant heating test (mode I, test 13) are presented in figure 16. The thermocouple locations at a depth of $z = 1.59$ cm are indicated in the sketch. The gap temperatures are compared with the calculated temperature in solid RSI at the same depth as shown by the dashed curve. The corresponding tile surface temperature history is also presented. The measured temperatures in the gaps due to radiant heating are about the same as those predicted for the tile interior.

The temperature histories from the same group of gap thermocouples are presented in figure 17 from an aerodynamic heating test (mode II, test 5). In this case, the gap temperatures are greatly affected by aerodynamic flow penetration and are much higher than the calculated temperatures of the tile interior at $z = 1.59$ cm. The temperature response in the longitudinal gaps was much greater than that in the lateral gaps, and the temperature in the longitudinal gap at location B1 was even greater than the surface temperature. The higher temperatures at B1 probably indicate flow penetration through the border joints.

The gap temperature distributions over the panel are shown on plan views of the tile array in figure 18 from a mode III test (test 8). The temperatures displayed in figure 18(a) were obtained after 1100 seconds of radiant heating, and the temperatures shown in figure 18(b) were obtained after 40 seconds of aerodynamic heating ($t = 1215$ seconds). Generally, the gap temperatures under radiant heating (fig. 18(a)) were between 762 K and 983 K as compared with an upper surface temperature of approximately 1100 K. However, as indicated in figure 18(b), the gap temperatures increased radically during the aerodynamic heating phase of the test. Temperatures near 1400 K were recorded along the longitudinal border gaps (rows 1 and 5), and temperatures of the interior gaps (rows 3, C, and G) were generally around 900 K to 1000 K. High temperatures are also indicated at the tee intersections at locations A3, E3, and I3. For example, the average temperature at E3 was 1336 K. The gap temperatures at these intersections were expected to be higher than the other gap temperatures because the forward-facing wall at the end of the longitudinal gap was a stagnation surface for gap flow. (See ref. 11.) The temperatures in the lateral gaps adjacent to the tee intersections in rows A, E, and I are from 100 K to 200 K less than those at the intersections but are generally greater than the interior gap temperatures.

Effects of Δp.- In the aerodynamic heating phases of the present tests, high temperatures in some of the tile gaps and in some regions of the substructure near joints were caused by flow leakage produced as a function Δp. The panel was aerodynamically loaded by reducing the cavity pressure to a value below the surface pressure. The Δp recorded in table II ranges from 0.11 to 8.41 kPa which is well below the entry design value of $\Delta p = 10.4$ kPa (ref. 6). In the present tests, the force of Δp produced considerable flow penetration into the tile gaps and joints around the subpanel edges but the interior gaps of the subpanels were not appreciably affected.

Flow penetration occurred in the area of the deep thermal seal which was bonded to the substructure frame in the joint between the subpanels at row E. The joint is described in figure 5(c). The flow-penetration effect of Δp is demonstrated in figure 19, where the gap and substructure temperatures along row E are presented as a function of Δp. These temperatures, which were taken from the five mode III tests at $\alpha = 15^\circ$ after

10

40 seconds of aerodynamic heating, show a linear variation with Δp to 7.67 kPa. At location E3 the gap temperatures (open square and diamond symbols) remained constant with Δp at an average value of 1336 K, which is substantially higher than the tile surface temperature. The substructure temperature at location E3 (solid square symbol) also remained constant and indicated that the thermal seal at this location prevented direct flow penetration. However, the gap temperatures at locations E2 and E4 (open circle and triangular symbols) and the substructure temperatures at locations E1 and E5 (solid circle and triangular symbols) increased significantly with Δp. Thus, a definite path of gas leakage was established along the lateral gap in row E to the gap locations E1 and E5 where penetration was made to the substructure.

Additional evidence of gas leakage was obtained when the subpanels were removed after these tests. The photographs in figure 20 show the panel with the forward subpanel removed. Much of the fibrous thermal seal was damaged during disassembly. Note that the deep, subpanel joint seal does not extend to the corner E5 where the highest substructure temperature was observed. (See fig. 19.) In this corner, gas leakage caused considerable erosion of the seal and of the silicone rubber bonding material. Therefore, in the present test, these seals did not provide adequate thermal protection to the substructure in the presence of differential pressure.

Tile Damage Tolerance

During the test series, the tiles incurred considerable surface damage such as particle impact craters, coating cracks, and tile erosion. In spite of the surface damage, the tile array still provided good thermal performance and appeared to have good structural integrity. The overall appearance of the tile surface at the conclusion of the tests is shown in figure 21. Since much of the damage occurred early in the test program, an opportunity was available to gain some insight into the damage tolerance of the LI-1542 material.

Particle impact craters.- During aerodynamic heating, the panel was bombarded by very small particles in the test stream which were produced from the flaking of an aluminum oxide coating from the facility combustor liner. Impact of these particles caused extensive crater damage to the tiles when the panel holder was pitched to an angle greater than zero. The size of the craters ranged from approximately 0.5 to 20 mm, and the estimated number of craters per tile at the end of the test series was 1000. A photomicrograph of a typical crater is presented in figure 22. The crater length and depth were about 4 mm. This crater was produced during test 12 but was photomicrographed after test 23. The tile coating at the edge of the crater is sharp and jagged which indicates that the impact caused a clean fracture of the coating. The appearance of the edges

of the coating also indicates that the aerodynamic flow of subsequent tests did not produce appreciable erosion or fire polishing of the edges.

A series of photographs are shown in figure 23 to illustrate the progression of surface damage caused by the particle impact. The photographs were taken of the same tile after tests 8, 12, and 23. The large crater (see location A in fig. 23(a)) appeared after test 8. It was field repaired with a mixture of the coating material, and no further erosion was experienced. A second large crater appeared after test 12 adjacent to the first large crater. (See fig. 23(b).) This crater was also repaired and both of the repaired craters can be seen intact in figure 23(c). A smaller crater (see location B in fig. 23(a)) also appeared after run 8. It was not repaired and showed no evidence of erosion for the remainder of the tests. Thus, small particle impact which caused craters in the RSI tiles had no discernible effect on tile integrity.

Coating cracks.- Cracks in the tiles, which were invisible to the naked eye, were detected at the beginning of the test program by wetting the surface with a volatile solvent. Actually, the first cracks were detected during panel inspections prior to initiating the first thermal cycle. A typical crack pattern in tile III (fig. 7(a)) is illustrated in figure 24. The crack pattern obtained prior to test 4 is shown in figure 24(a). After test 4, all the tiles were crazed similar to the tile shown in figure 24(b), but the crazing did not worsen with repeated testing. Test 4 was a mode II test in which the panel, at ambient temperature, was inserted into the hot, wind-tunnel stream. This test was the first mode II test that was conducted at the most severe test condition, but combustor flameout occurred after about 6.2 seconds of testing. The total temperature of the stream dropped to about the ambient temperature level as the panel was being removed from the stream. Thus, the panel experienced rapid heat-up and cool-down in this test. The results of the thermal stress analysis presented in appendix B for the two extreme temperature gradients indicated that tensile stress in the tile coating associated with a rapid cool-down was about 83 percent of the allowable stress. Consequently, the failure of the coating was probably due to factors other than thermal stress alone. Although the tile coating was badly crazed, the tiles demonstrated good structural integrity and surface toughness throughout the remainder of the test program.

Since a tile with crazed coating would be vulnerable to water ingress, two tiles were soaked with water for test 23 to determine the effect of water on tile integrity during rapid change in surface pressure and temperature. Tiles VI and VIII contained 0.2 and 0.1 kg of water, respectively. At the beginning of the test, the surface pressure was reduced from about 100 kPa (atmospheric pressure) to 1.5 kPa in about 10 seconds. The depressurization rate in these tests was far more severe than would be expected on an actual launch of the space shuttle. When the panel was in the stream, the surface pressure was about 14.7 kPa (table III). The water-soaked tiles experienced some damage

12

in the form of flaking of the coating as shown in figure 25. The flaking occurred mostly in the outer layer of the coating as shown on the right side of the photograph, but in some cases the flakes were deep enough to expose the insulation as shown on the left side. Although the flaking could have occurred along existing cracks, the typical flake damage differs in size and shape from the crazed areas such as those outlined in the crazed coating of figure 24. All the flaking occurred on the top surface within about 2 cm of the tile edges. This flaking is similar to that described in reference 12 as eruptions of the coating which occurred during thermal cycles of uncracked tiles after they had been exposed to water. As indicated in reference 12, eruption of flakes could have been caused either by outgassing of water vapor or by outgassing from oxidation of silicon carbide in the outer layer of the coating in the presence of water vapor. Therefore, the presence of water seems to be the key factor in producing coating eruptions in reference 12 and in the present test 23. The localized coating eruptions would decrease the reusability of the RSI tiles, but the damaged coating appears to be strong enough to prevent a catastrophic failure of the tile.

Erosion.- Most of the tile erosion occurred on forward-facing steps and forward-facing walls at the ends of longitudinal gaps. The erosion was closely associated with particle impacts. It appeared that the tough coating of the tiles seldom eroded from flow shear alone. However, if the coating was initially broken by particle impact which exposed the insulation (LI-1500), the insulation was then susceptible to further damage from flow shear and from additional particle impacts. In some instances the flow eroded the exposed insulation from beneath the coating and caused sections of the unsupported coating to break, apparently by aerodynamic forces.

The most extensive erosion of a forward-facing step occurred along row I. The progression of the edge erosion of the 0.4-mm step is shown in figure 26. A large crater was produced in the tile edge during test 4 and was repaired (fig. 26(a)). Considerable erosion occurred during test 5 (fig. 26(b)), and the tile edge continued to erode in each successive aerodynamic exposure. At the conclusion of test 23 the panel had been exposed to 403 seconds of high shear flow, and erosion had progressed as much as 4 cm from the edge (fig. 26(c)).

Typical erosion damage to the forward-facing walls of both subpanels at the ends of longitudinal gaps at locations A3 and E3 is shown in figure 27. Location A3 is at the end of a gap 18 cm long, whereas location E3 is at the end of a gap 58 cm long. (See fig. 7.) The erosion damage at A3 (fig. 27(a)) is less severe than at E3 (fig. 27(b)) and includes a number of small holes through the coating that were apparently produced by particle impact. At E3, both the upper edge of the tile and the wall were damaged by considerable erosion of coating and insulation materials. The upper edge of the tile eroded at this location because it formed a 0.6-mm forward-facing step, and the erosion in the wall

produced a hole 1 cm deep within which melted silica fibers were seen. A photomicrograph of the erosion hole is presented in figure 28(a). Scanning electron micrographs of the insulation are presented in figures 28(b) and 28(c) for a magnification of about ×680. It is apparent from figure 28(b) that the silica fibers at position "A" have been melted when compared with the undamaged fibers (fig. 28(c)) taken from unexposed areas near the damaged hole. However, the maximum stagnation temperature obtainable in the facility is too low to melt silica fibers. The melted fibers shown in figure 28(b) may have resulted from increased temperature associated with particle impact. Although it is clear that flow in longitudinal gaps stagnating on forward-facing walls is a source of high local heating (see ref. 11), it appears that the stagnating flow would not have produced any erosion without particle impact.

Thermal Stresses in RSI Tile

In spite of all the surface damage incurred by the RSI tiles because of particle impacts, coating cracks, and erosion, the thermal performance and damage tolerance exhibited by the tiles demonstrates the capability of the test panel to withstand the loading conditions to which it was subjected. However, the application of this panel as a thermal protection system for a space shuttle vehicle will expose the panel to many additional types of loading conditions, one of which is a cold thermal soak in space. The analysis presented in appendix B includes the calculation of thermal stresses which occur as a result of subjecting the panel to a uniform 160 K temperature distribution. Results of the analysis for this loading condition indicate unacceptable shear stresses would occur because of the high stiffness properties of the RTV-560 strain isolator. These results suggest the need to consider other isolator materials. The use of Nomex felt as a strain isolator is of interest since, unlike RTV-560, Nomex is believed to remain flexible even at temperatures as low as 160 K. Analysis of a tile with Nomex felt as a strain isolator gives greatly reduced stress levels and indicates that on the basis of thermal stress alone, a significant increase in tile size may be possible. (See appendix B.) It must be recognized, however, that the analysis does not include the effects of other conditions such as pressure, dynamic and acoustic loads, and the consideration of a real, flexible vehicle substructure. Also, the results neglect the effect of a coating on the side edges of the tile. Each of these factors may significantly affect the maximum allowable tile size.

CONCLUDING REMARKS

A large panel of LI-1542 RSI tiles was subjected to a total of 23 cyclic heating tests by use of radiant lamps and aerothermal tests in the Langley 8-foot high-temperature structures tunnel to assess its thermal and structural performance. The test panel was

14

designed to represent a portion of the surface structure on a space shuttle orbiter fuselage along a 1250 K isotherm. Aerothermal tests were conducted at a free-stream Mach number of 6.6, a total temperature of 1820 K, Reynolds numbers of 2×10^6 and 5×10^6 per meter, and dynamic pressures of 26 and 65 kPa.

The RSI tiles demonstrated good thermal protection and good structural integrity. The thermal response of the RSI tile was repetitive and predictable with the use of a transient, one-dimensional analysis through the depth and a surface emissivity determined from the self-emission technique. However, high temperatures were recorded in the tile gaps and regions of the substructure due to flow leakage around thermal seals at joints in the presence of differential pressure. The damage tolerance of LI-1542 RSI appeared to be very high. Impact of foreign particles in the stream caused craters in the tiles, but field repairs successfully retarded erosion of the impacted area. The tile coating crazed early in the test program, but this did not affect tile integrity. Tiles with cracked coating were soaked with water and subjected to rapid depressurization and aerodynamic heating without any catastrophic failure, but small coating eruptions occurred along the tile edges. Considerable erosion of the tile edges occurred at forward-facing steps and at the ends of longitudinal gaps because of combined effects of particle impacts and flow shear. Results of stress analysis alone indicated that with a heat load uniformly applied over the top surface, a significant increase in tile size may be possible.

Langley Research Center
National Aeronautics and Space Administration
Hampton, Va. 23665
January 13, 1976

APPENDIX A

THERMAL ANALYSIS OF LI-1542 TPS

A thermal analysis was made to determine the temperatures at the surface and through the depth of an RSI thermal protection system to correlate with experimentally determined temperature distributions. The program used for the analysis was MITAS (Martin Interactive Thermal Analysis System) which uses a finite-difference solution as described in reference 13.

Analytical Model

The one-dimensional model used to compute the temperature distributions through the thickness of the RSI panel between supports is shown schematically in figure 29. The analytical model divided the thickness of the LI-1500 insulation into 11 nodes and used a single node each for the LI-0042 coating, RTV-560, beryllium subpanel, and the aluminum base plate. The analysis accounted for conduction through the system, and the modeling included a radiation and free convection interchange between the beryllium subpanel and the aluminum base plate. The subpanel cross section was simplified for this model by distributing the mass of the subpanel into an equivalent thickness of a single sheet of beryllium. This procedure did not appreciably affect the results because of the high conductivity of the beryllium and it simplified the inclusion of the free convection heating mode. The transient thermal analysis was performed by an explicit forward-differencing method.

Heat input to the model was varied for the different test modes. In the radiant heat test for modes I and III, the experimentally determined temperature history of the outer thermocouple located 1 mm deep in the RSI was used as a time-dependent boundary condition to define the heat input. In the aerodynamic heating test for modes II and III, the convective heat from the stream to the outer surface was determined from calibration results presented in reference 7. The temperature history of the base plate was another time-dependent boundary condition because the extraneous heat losses from the base plate would be very difficult to model analytically.

RSI Thermal Properties

The thermal properties for the various materials in the RSI test panel were obtained from references 6 and 9 and are presented in table IV. The properties of the RSI material were selected by assuming that the material is characteristic of a solid conductor. Actually, the material is very porous and is slightly translucent to radiation. The thermal properties were evaluated in the present tests by comparing the experimental and

analytical temperature distributions through the depth of the test panel presented in figure 30 for a mode I test (test 13). Results from six thermocouples are given: four embedded in the insulation, one attached to the beryllium subpanel, and one attached to the aluminum base plate. The predictions are indicated by the dashed curves and agree with experimental results with some deviation. At each depth the analysis underpredicted and then overpredicted the experiment with time. To indicate the sensitivity of the thermal properties of the RSI material in these calculations, the heat capacity and thermal conductivity were varied ±10 percent to account for a scatter range indicated in reference 9. These variations produced a band that improved agreement with experiment. Although the difference between experiment and analysis was not consistent, the published thermal properties appear to be adequate for predicting thermal response of the RSI interior.

RSI Surface Emissivity

In evaluating the thermal response of the RSI exposed to aerodynamic convective heating, the surface emissivity is a very important parameter. Published values of emissivity of the tile coating differ greatly for two measurement techniques. The emissivity as determined from the two techniques is presented in figure 31 as a function of temperature. The solid curve, taken from reference 9, was obtained by using a reflectance technique where the surface reflectance is measured and the emissivity is determined indirectly. The dashed curve with diamond symbols was taken from reference 10 and was obtained by using a self-emission technique where the emittance from the specimen temperature is varied. The scatter in the data from reference 10 is also indicated in the figure. Emissivity was also measured on specimens cut from the present test panel by use of the self-emission technique, and the results, indicated by the circular symbols, are in good agreement with those obtained from reference 10.

Thermal analyses were made for the mode II test by use of the different values of emissivity, and the results are presented in figure 32. The temperature histories of the test panel are presented for a mode II test (test 5) which consisted of 30 seconds of aerodynamic heating. In the figure the solid symbols are surface temperature data obtained from the infrared radiometer. The open symbols are data obtained from the thermocouples located at various insulation depths. The solid curves are the thermal response for the corresponding depth locations predicted by using the surface emissivity of reference 10 (self-emission technique). These predictions are in excellent agreement with the temperature indicated by both the radiometer and the embedded thermocouples. However, the experimental data do not agree with the predictions based on the emissivity of reference 9. Thus, the correlation of the radiometer and thermocouple data with the two sets of predictions in figure 32 indicates better agreement when the surface emissivity obtained with the self-emission technique is used.

APPENDIX B

THERMAL STRESS ANALYSIS OF AN LI-1542 RSI TILE

A simplified thermal stress analysis of an LI-1542 RSI tile was conducted to assess the response of the tile coating, insulation, strain isolator, and metal support structure to thermal loads imposed during the test program. The analysis was performed by using SNAP (Structural Network Analysis Program, ref. 14), a two-dimensional finite-element digital computer program. The material properties used in the analysis were obtained from references 9, 15, and 16 and are given in table V.

Analytical Model

Figure 33 shows a typical LI-1542 RSI tile and the portion of the tile which was modeled. A vertical slice of half of the tile (see fig. 33(a)) with a thickness arbitrarily selected to be 0.025 cm was modeled with finite elements as shown in figure 33(b). This approach to modeling the tile assumes that the panel is in a state of plane stress. Conditions of symmetry were imposed along the edge from joints 1 to 11, and joint 11 was completely restrained from translation or rotation. The bottom of the beryllium panel (joints 11, 22, 33, . . ., 231) was held flat but was allowed to translate in the x-direction. All elements are quadrilateral membrane elements unless otherwise specified. Figure 33(c) shows the finite-element grid that included a rudimentary model of the thin coating. The membrane elements in the top row were replaced with rod elements which were connected to the membrane elements by shear panels. The shear panel elements transmit load between the rod and membrane elements and were assigned a high modulus of elasticity to simulate a rigid attachment between the coating and the insulation. Short rods (not shown in fig. 33(c)) were also used to stiffen the short sides of the shear panel elements, for example, between joints 1 and 2, 12 and 13, etc. For simplicity, the side-wall coating was not modeled. The sidewall coating was assumed to have negligible effect on stresses in the top surface, since the coating, observed after test 4, was uniformly crazed over the top surface. However, other environments to which the panel might be exposed such as a cold soak in space may result in significant effects from the sidewall coating.

Thermal Stress in RSI Coating

To assess the cause of the crazed coating observed after test 4 (see fig. 24), the tile was analyzed for two temperature conditions which occur as a result of the sudden heat-up and cool-down imposed on the RSI during test 4. These two conditions were as follows: (1) the coating temperature was 1144 K and the insulation was at a uniform 295 K, which was the most severe temperature difference possible for causing compres-

18

sive thermal stress in the coating and, (2) the coating temperature was 295 K and the insulation was at a uniform 1144 K, which was the most severe case for causing tensile thermal stress in the coating. These temperature conditions are extreme, and it is reasonable to assume that these temperatures produce upper limits to the thermal stress in the coating.

The ratios of the maximum thermal stresses in the coating and in the insulation to their respective ultimate stresses were calculated for the two extreme temperature distributions and are shown in figure 34. Ultimate stresses for the coating and insulation in both tension and compression are given in the figure. The maximum stress in the coating occurs at the center of the tile, and the maximum stress in the insulation occurs at the tile edge. Calculated stresses in the coating and the insulation are not great enough to cause failure in either tension or compression. However, the maximum coating stress is 83 percent of its ultimate tensile stress. This thermal stress, in combination with stresses unaccounted for by the analysis such as those produced by aerodynamic pressure, dynamic loads, or those due to nonuniform thickness of the coating, may have been sufficient to cause the coating to craze.

Thermal Stresses in Tile With Crazed Coating

When the coating becomes crazed, the crack pattern divides the surface of the coating into many relatively small areas. It is assumed that these small areas are structurally isolated from each other and that they do not transmit inplane loads. Thus, it is assumed that the analysis of a tile without a coating is representative of the analysis of a tile with a crazed coating. Accordingly, the following results for a tile with a crazed coating were obtained by analyzing a tile with the coating neglected.

A thermal stress analysis was conducted on the tile with temperature distributions representative of a space shuttle entry mission. The first temperature distribution selected for analysis was a uniform 160 K cold soak condition. A second temperature distribution selected was nonlinear and was calculated based on the typical surface temperature history for a space shuttle entry shown in figure 35(a). During entry, the surface temperature increases from a cold soak condition in space at 160 K to 1144 K in about 480 seconds. The condition identified in figure 35(a) at $t = 480$ was selected for analysis because it offers potentially critical thermal stresses arising from a combination of constrained thermal growth, and a large nonlinear temperature gradient through the thickness. A temperature gradient was calculated for the time at 480 seconds by use of the MITAS thermal analysis computer program described in appendix A and is shown in figure 35(b).

Thermal stresses were calculated for the uniform 160 K condition and for the entry temperature gradient shown in figure 35(b). Results of these analyses, which neglect the

coating, are shown in figure 36. In the 160 K cold soak case the RTV-560 strain isolator was ineffective and resulted in a shear stress at the interface between the insulation and the strain isolator near the tile edge almost 300 percent of the ultimate shear strength. This unacceptable shear stress occurs because RTV-560 increases in stiffness by greater than one order of magnitude when it is cooled from room temperature to 160 K (ref. 17), which seriously reduces its effectiveness as a strain isolator.

Thermal stresses arising from the 1144 K to 160 K temperature gradient are given in figure 36(b). All stresses are well below critical values. The low stresses result, in part, from the assumption that the RTV-560 undergoes stress relaxation prior to the tile being exposed to entry conditions. This assumption is based on data which show that RTV-560 undergoes a 90-percent stress relaxation at 160 K, most of which occurs in a relatively short period. (See ref. 17.)

Effect of Tile Size on Thermal Stress of RSI With

Nomex Felt Strain Isolator

It is anticipated that the stress level in the tiles will increase with increased tile size. However, the use of RTV-560 as a strain isolator for larger tiles will lead to even less acceptable shear stresses under a cold soak condition. The need exists, therefore, to consider other isolator materials. The use of Nomex felt as a strain isolator is of interest since, unlike RTV-560, Nomex is believed to remain flexible even at 160 K. An RSI tile with a Nomex strain isolator bonded to a beryllium panel of the same size as previously studied except with slightly different strain isolator thicknesses (0.254 cm Nomex) was analyzed for the same cold soak temperature condition. The results are shown in figure 37. Comparison of these results with those for the beryllium RTV-560 subpanel (fig. 36(a)) shows a large reduction in RSI stresses and suggests that larger tile sizes may be acceptable.

An indication of the effect of tile size on thermal stresses is shown in figure 38. Figure 38(a) shows the maximum inplane stress σ_x and shear stress τ_{xz} as a function of tile size for the cold soak condition, and figure 38(b) shows the same stresses for the entry temperature gradient given in figure 35(b). The solid lines are stresses for the coated tile, and the dashed lines represent the stresses for the tile with a crazed coating. In all cases the stresses increase with increasing tile size. The σ_x stresses shown in figure 38(a) are at the bondline of the RSI. The stresses in the RSI with coating are less than those in the tile with a crazed coating. The coating causes additional compressive stresses in the RSI at the top of the tile and changes the stress distribution so that the maximum stress at the bondline is reduced. In figure 38(b) the maximum σ_x stresses are also compressive but are at the top of the RSI. Because the coating has a higher coefficient of thermal expansion than the insulation, the coating causes tensile

20

stress in the insulation and reduces the maximum compressive stress. Furthermore, because the coating has higher modulus of elasticity than the insulation, it tends to carry a greater share of the compressive load; thus, further reduction of the stresses in the insulation with the coating results.

The effect of the coating on shear stresses is small for the cold soak condition (fig. 38(a)), but it is larger for the entry temperature gradient condition (fig. 38(b)). The maximum shear stresses occur near the tile edge and near the bondline. The coating is subjected to a large temperature change which combines with a high coefficient of thermal expansion to increase the thermal growth of the tile. This increase in thermal growth causes the increase in shear stress.

Examination of figure 38 indicates that the thermal stresses for a 60-cm-square tile are well within acceptable limits whether the coating is crazed or not. Thus, even larger tiles are acceptable if a strain isolator such as Nomex is used. It must be recognized, however, that these results do not include the effects of other conditions such as pressure, dynamic and acoustic loads, and the consideration of a real, flexible vehicle substructure. Also, these results neglect the effect of a coating on the side edges of the tile. Each of these factors may significantly affect the maximum allowable tile size.

REFERENCES

1. Anderson, Roger A.; Brooks, William A., Jr.; Leonard, Robert W.; and Maltz, Joseph: Structures − A Technology Overview. Astronaut. & Aeronaut., vol. 9, no. 2, Feb. 1971, pp. 38-47.

2. Love, Eugene S.: Advanced Technology and the Space Shuttle. Astronaut. & Aeronaut., vol. II, no. 2, Feb. 1973, pp. 30-66.

3. Deveikis, William D.; Miserentino, Robert; Weinstein, Irving; and Shideler, John L.: Aerothermal Performance and Structural Integrity of a René 41 Thermal Protection System at Mach 6.6. NASA TN D-7943, 1975.

4. Bohon, Herman L.; Sawyer, J. Wayne; Hunt, L. Roane; and Weinstein, Irving: Performance of Full Size Metallic and RSI Thermal Protection Systems in a Mach 7 Environment. AIAA Paper No. 75-800, May 1975.

5. Hunt, L. Roane; and Bohon, Herman L.: Performance of LI-1542 Reusable Surface Insulation System in a Hypersonic Stream. NASA TM X-71955, 1974.

6. Burns, A. Bruce: Structural Evaluation of Candidate Space Shuttle Thermal Protection Systems. NASA CR-132428, 1972.

7. Deveikis, William D.; and Hunt, L. Roane: Loading and Heating of a Large Flat Plate at Mach 7 in the Langley 8-Foot High-Temperature Structures Tunnel. NASA TN D-7275, 1973.

8. Deveikis, William D.; Bruce, Walter E., Jr.; and Karns, John R.: Techniques for Aerothermal Tests of Large, Flightweight Thermal Protection Panels in a Mach 7 Wind Tunnel. NASA TM X-71983, 1974.

9. Space Shuttle Thermal Protection System Development. Vol. I. LMSC-D152738 (Contract NAS 9-12083), Lockheed Missiles & Space Co., Inc., Jan. 17, 1972. (Available as NASA CR-115582.)

10. Kantsios, Andronicos G.; Edwards, S. Franklin; and Dicus, Dennis L.: Spectral and Total Normal Emittance of Reusable Surface Insulation Materials. Symposium on Reusable Surface Insulation for Space Shuttle, Vol. I, NASA TM X-2719, 1973, pp. 327-347.

11. Weinstein, Irving; Avery, Don E.; and Chapman, Andrew J.: Aerodynamic Heating to the Gaps and Surfaces of Simulated Reusable-Surface-Insulation Tile Arrays in Turbulent Flow at Mach 6.6. NASA TM X-3225, 1975.

12. Ransone, Philip O.; and Morrison, J. D.: The Effects of Environmental Exposure on Reusable Surface Insulation for Space Shuttle. NASA TM X-3252, 1975.

13. Martin Interactive Thermal Analyzer System — Version 1.0. User's Manual. MDS-SPLPD-71-FD238 (REV 3), Martin Marietta Corp., Mar. 1972.

14. Whetstone, W. D.: Structural Network Analysis Program — User's Manual. Static Analysis Version V70E. LMSC-HREC D162812. Lockheed Missiles & Space Co., Dec. 14, 1970.

15. Buttram, R. D.: Development of a Rigidized, Surface Insulative Thermal Protection System for Shuttle Orbiter. MSC-02567 (Contract No. NAS 9-11222), Lockheed Missiles & Space Co., Feb. 16, 1971. (Available as NASA CR-114958.)

16. Aerospace Structural Metals Handbook. AFML-TR-68-115, U.S. Air Force, 1975.

17. Owen, H. P.; and Carroll, M. T.: Development of Design Allowables Data for Adhesives for Attaching Reusable Surface Insulation. NASA CR-128887, 1972.

TABLE I.- UNIT MASS OF TPS TEST PANEL COMPONENTS

Component	Unit mass, kg/m^2, for –		
	Front subpanel	Rear subpanel	Average
LI-1542 tiles	8.69	7.68	8.18
FI-600	0.21	0.21	0.21
RTV-560 bond	3.36	3.36	3.36
Beryllium subpanel	4.71	4.66	4.68
Total	16.97	15.91	16.43
Corresponding LI-950 shuttle baseline			≈10.0

TABLE II.- TEST SEQUENCE AND TEST CONDITIONS OF THE LI-1542 PANEL

Test	Mode	Radiant heat			Aerodynamic heat				Comments
		Heat-up time, s	Constant temperature time, s	Surface temperature, K	Time in stream, s	Surface temperature, K	Δp, kPa	α, deg	
1	I	340	350	1240					
2	II				2.8	370	0	0	Flow breakdown
3	II				45.8	720	.14	0	
4	II				6.2	910	8.41	15	Combustor flameout
5	II				30.8	1100	8.25	15	
6	II				43.3	1120	8.16	15	
7	I	380	780	1090					
8	III	380	790	1120	40.6	1190	7.15	15	
9	I	380	1270	1090					
10	III	430	670	1090	39.2	1180	6.69	15	
11	III	460	950	1090	40.6	940	-.92	0	Model radiant heat to 1090 K was based on test $\alpha = 15^\circ$
12	III	440	650	1040	40.4	1160	4.94	15	
13	I	530	1410	1090					
14	I	450	630	1080					
15	III	420	650	1090	40.6	1170	7.67	15	
16	I	450	1280	1100					
17	I	430	650	1090					
18	I	440	620	1080					
19	I	430	960	1100					
20	I	450	160	1070					
21	I	410	1800	1050					
22	III	430	1070	1080	40.6	1190	.11	15	
23	II				31.7	1120	.11	15	Two tiles soaked with water prior to test

TABLE III.- FLOW CONDITIONS OF AERODYNAMIC HEATING

TEST OF THE LI-1542 PANEL

Test	Free stream					Local		
	T_t, K	R_L, m^{-1}	q_∞, kPa	M_∞	p_∞, kPa	q_l, kPa	M_l	p_l, kPa
2	1790	2.14×10^6	26.3	6.8	0.83	26.3	6.8	0.83
3	1790	2.14	26.3	6.8	.83	26.3	6.8	.83
4	1770	5.23	65.2	6.5	2.17	176	4.2	14.9
5	1830	4.99	64.8	6.6	2.12	175	4.2	14.7
6	1810	5.05	65	6.6	2.14	175	4.2	14.7
8	1830	4.98	65	6.6	2.14	175	4.2	14.7
10	1830	4.94	65	6.6	2.14	175	4.2	14.7
11	1820	5.02	64.9	6.6	2.14	64.9	6.6	2.14
12	1810	5.05	65	6.6	2.16	175	4.2	14.8
15	1820	5.13	65	6.6	2.14	175	4.2	14.8
22	1820	4.96	64.1	6.6	2.12	173	4.2	14.6
23	1800	5.15	64.8	6.6	2.14	174	4.2	14.7

TABLE IV.- THERMAL PROPERTIES OF MATERIALS IN RSI TEST PANEL

Material property	LI-0042 (a)		LI-1500 (a)		RTV 560 (a)		Beryllium (b)	
	295 K	1367 K	295 K	1367 K	295 K	528 K	295 K	589 K
k, W/m-K:								
p = 0.34 kPa	0.94	2.05	0.024	0.096	---	---	---	---
p = 2.57 MPa	0.94	2.05	0.050	0.225	0.28	0.22	180	142
C_p, kJ/kg-K	0.63	1.34	0.63	1.34	1.26	---	1.86	2.57

[a]Reference 9.
[b]Reference 6.

TABLE V.- PHYSICAL PROPERTIES OF TPS MATERIALS

Physical property	LI-0042 coating (a)	LI-1500 insulation at — 1144 K (a)	LI-1500 insulation at — 160 K (a)	RTV-560 at 160 K (a)	Nomex at 160 K (b)	Beryllium (c)
E_x, GPa	13.1	0.144	0.074	0.111	0.003	155
E_z, GPa	13.1	0.030	0.022	0.111	0.00016	155
G, GPa	------	0.014		0.041	0.000042	73.8
α, m/m-K	7.2×10^{-7}	6.5×10^{-7}		0.18×10^{-7}	0	112×10^{-7}
Tension:						
$\sigma_{x,ult}$, kPa	6 895	207		6 895	------	------
$\sigma_{z,ult}$, kPa	6 895	55		6 895	------	------
Compression:						
$\sigma_{x,ult}$, kPa	41 400	896		------	------	------
$\sigma_{z,ult}$, kPa	41 400	275		------	------	------
$\tau_{xz,ult}$, kPa	--------	55		4 800	------	------

[a] Interpreted from references 9 and 15.
[b] Unpublished data.
[c] Reference 16.
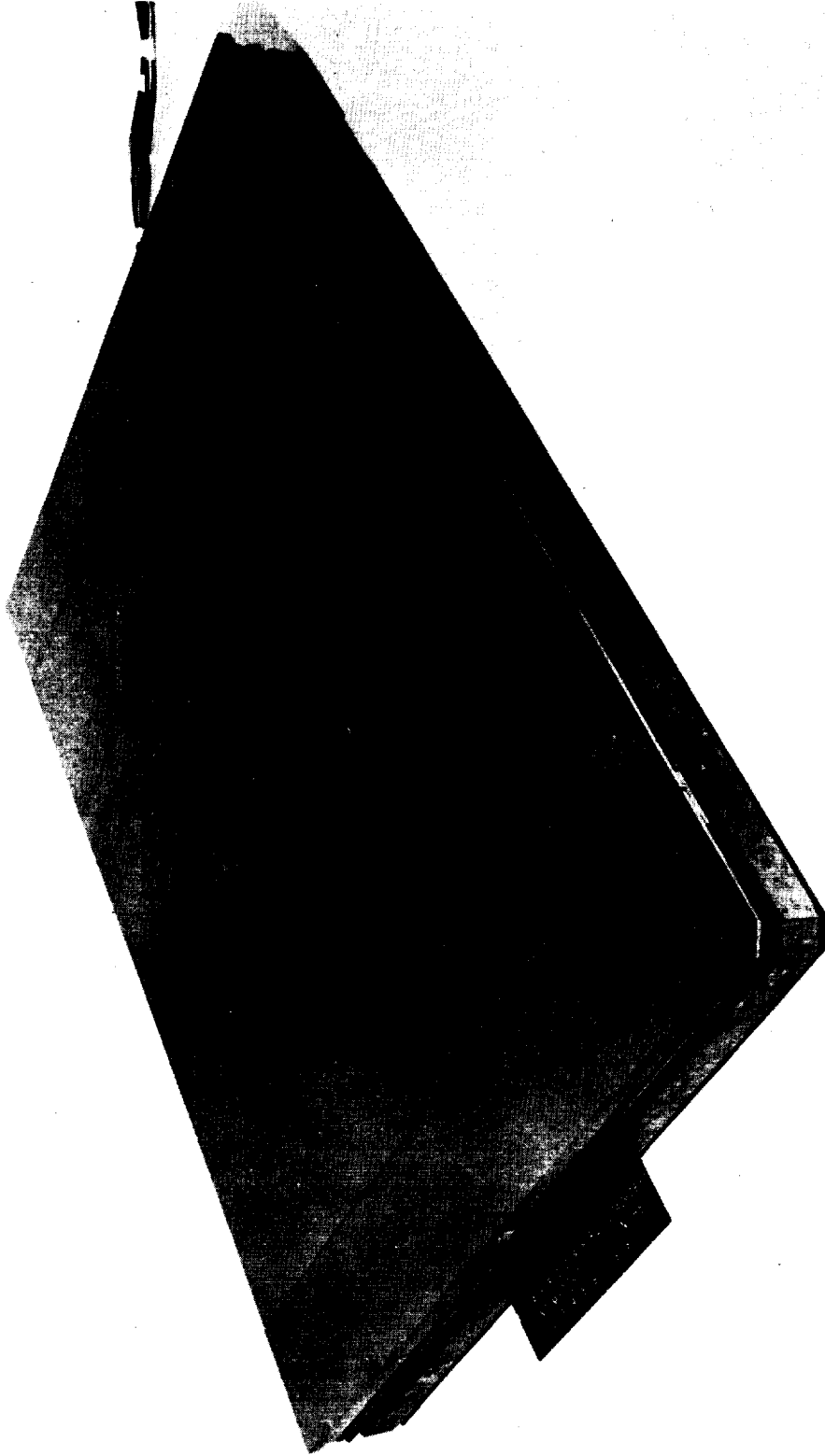
Figure 1.- Test panel with RSI tiles.

L-72-4143

29
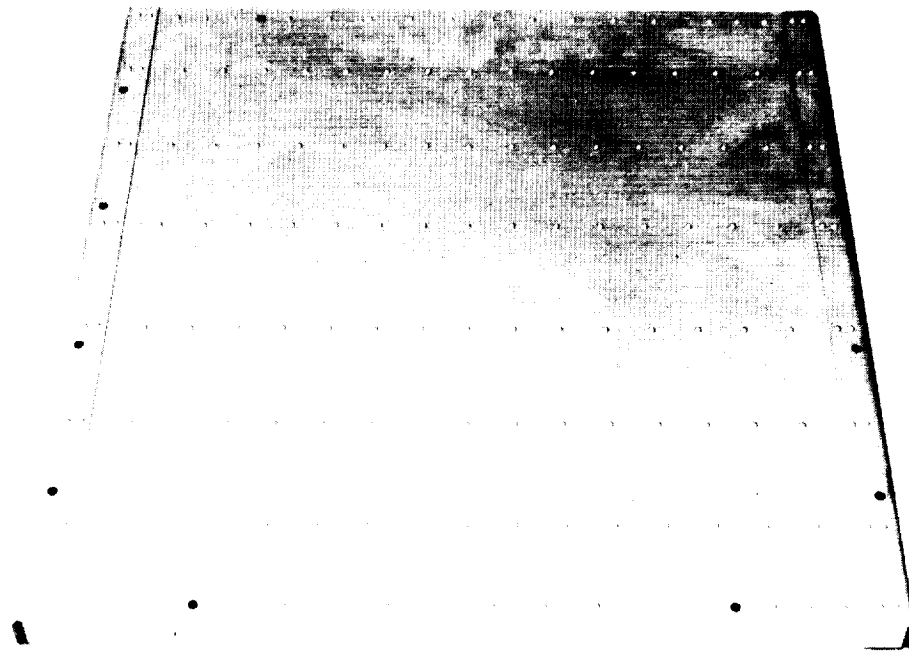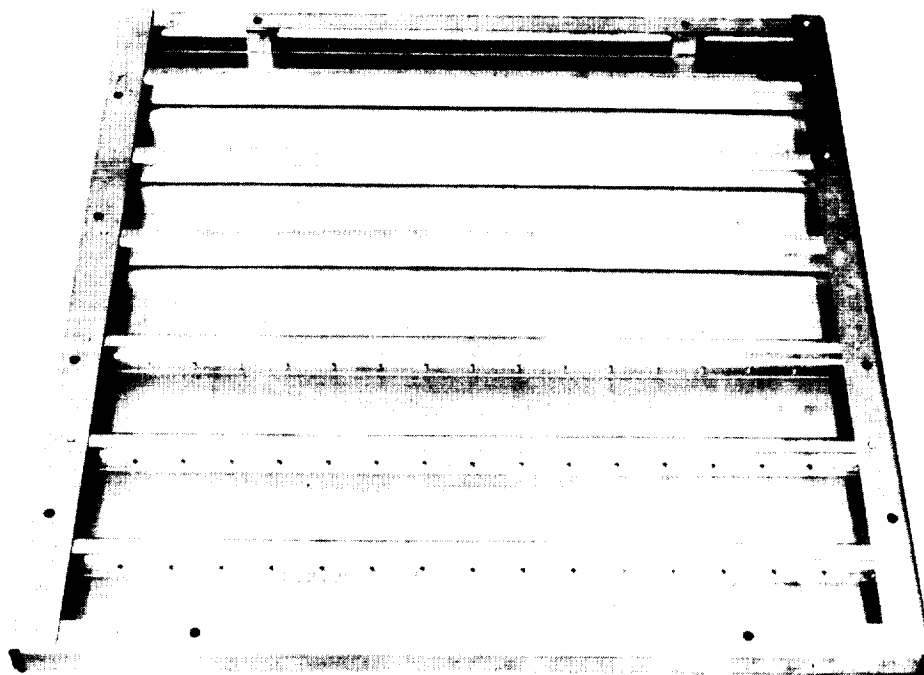
(a) Top view.

(b) Bottom view.

L-76-101

Figure 2.- Stringer-stiffened beryllium subpanel.

Cover plate
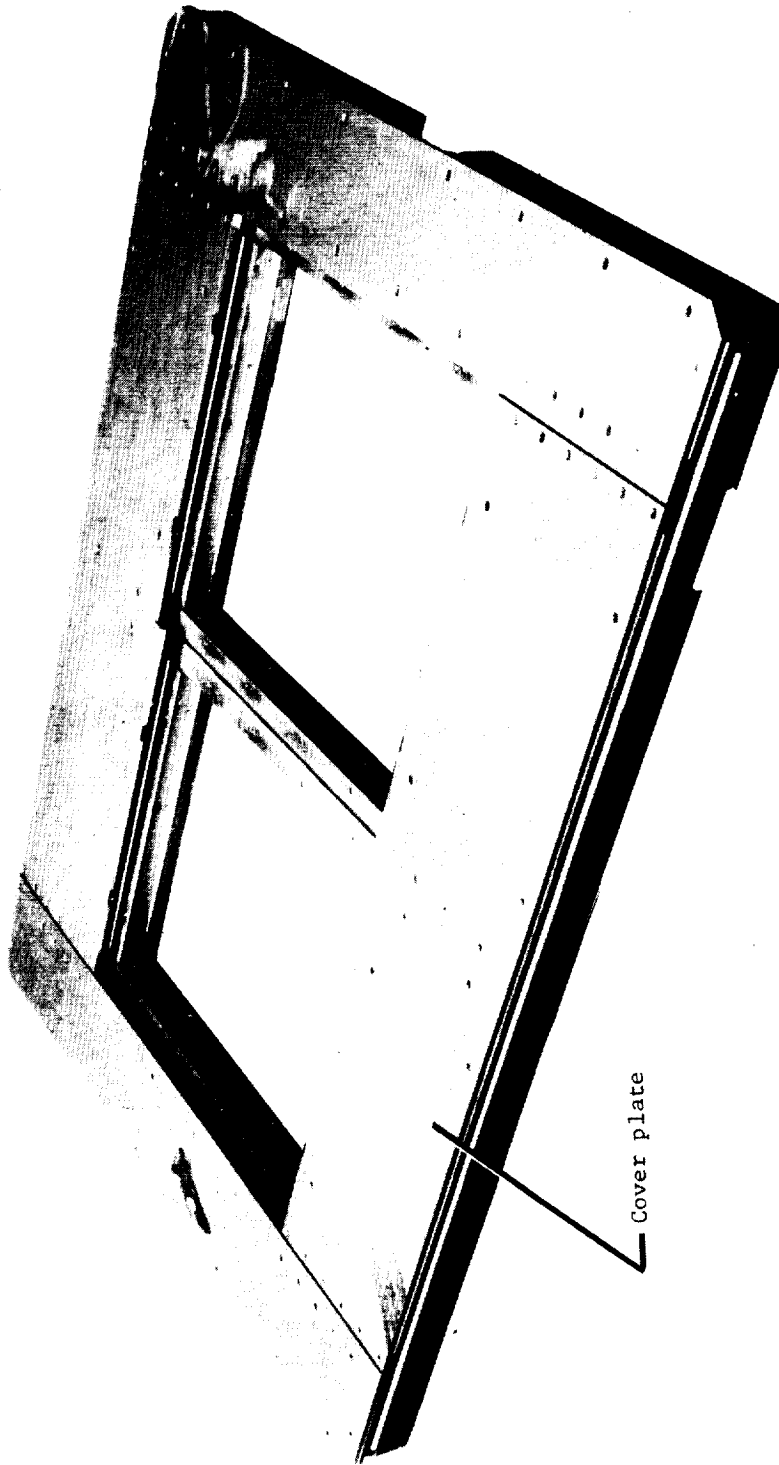
(a) Top view.

Figure 3.- Titanium frame.
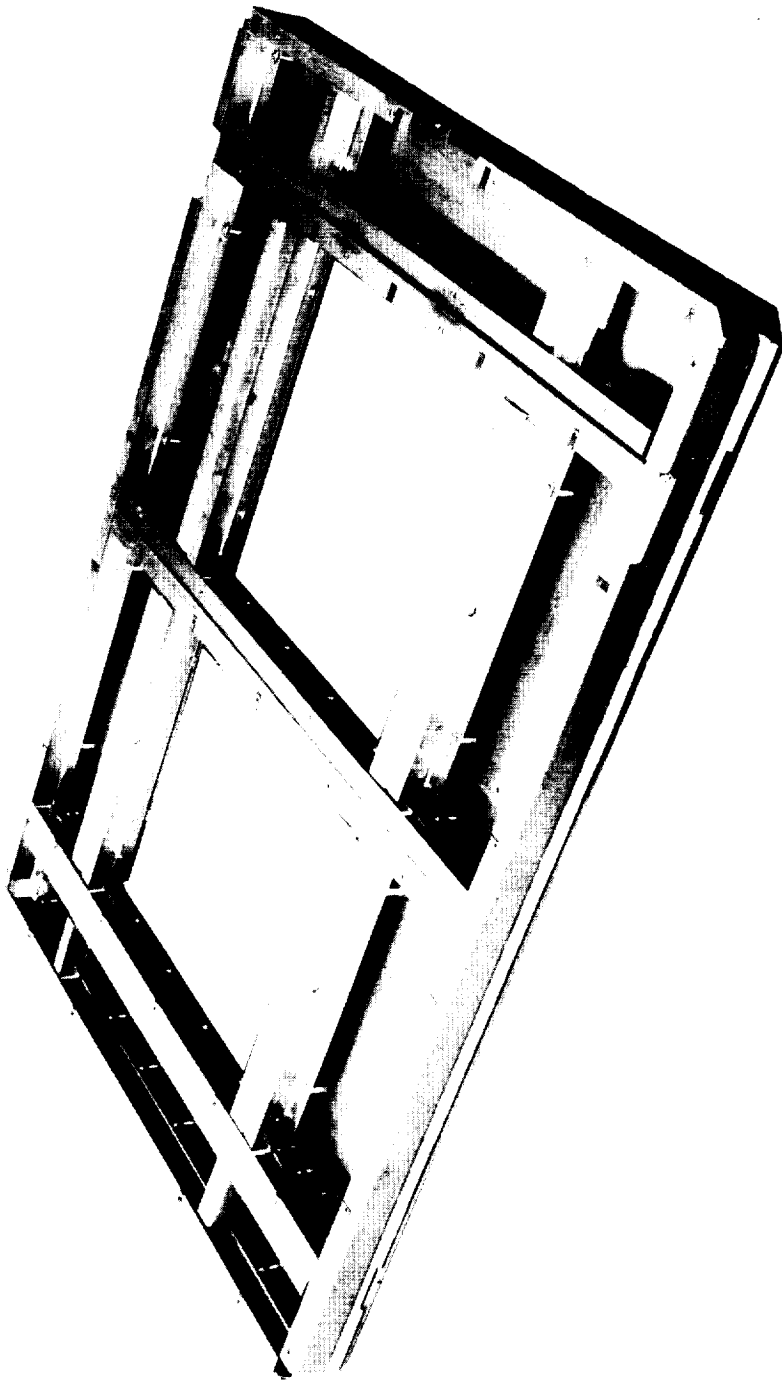
(b) Bottom view.

Figure 3.- Concluded.

L-76-103

32
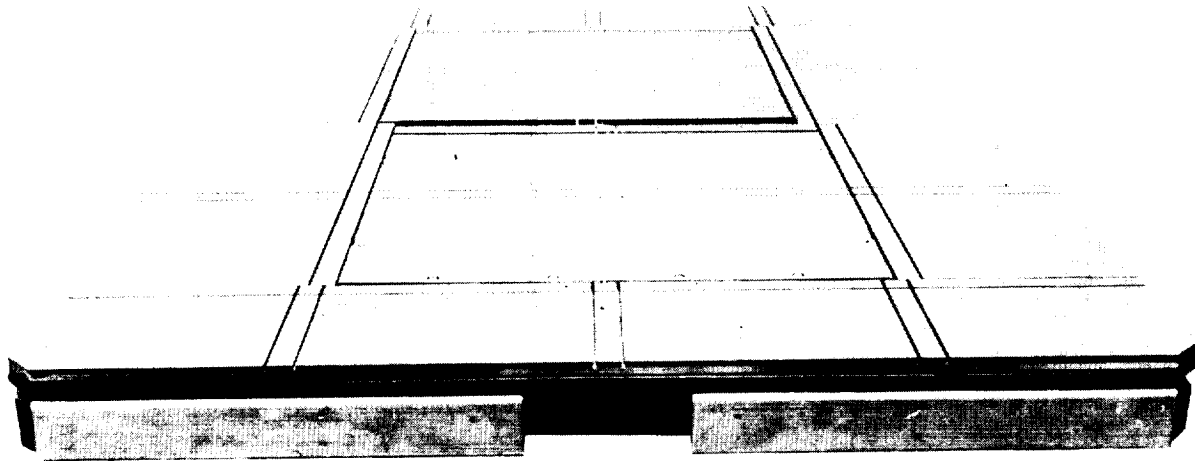
(a) Substructure with grooved strain isolator.
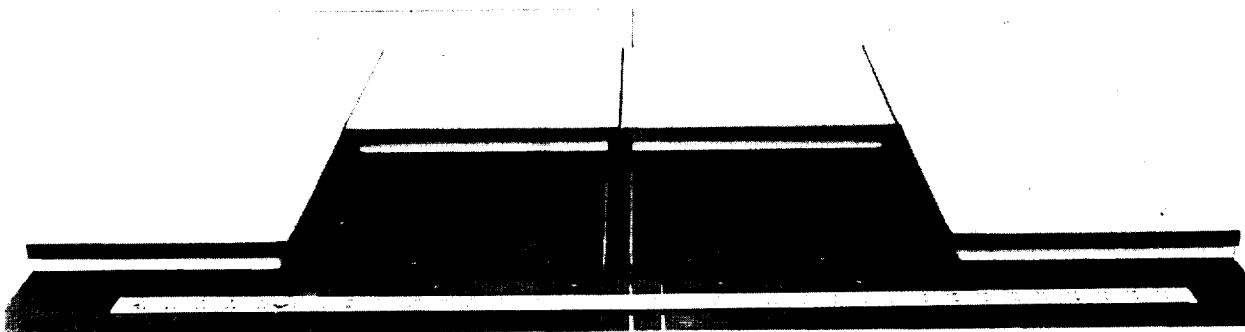
(b) Tile placement.

L-76-104

Figure 4.- Tile assembly.

(a) Border joint.

(b) Interior gap.
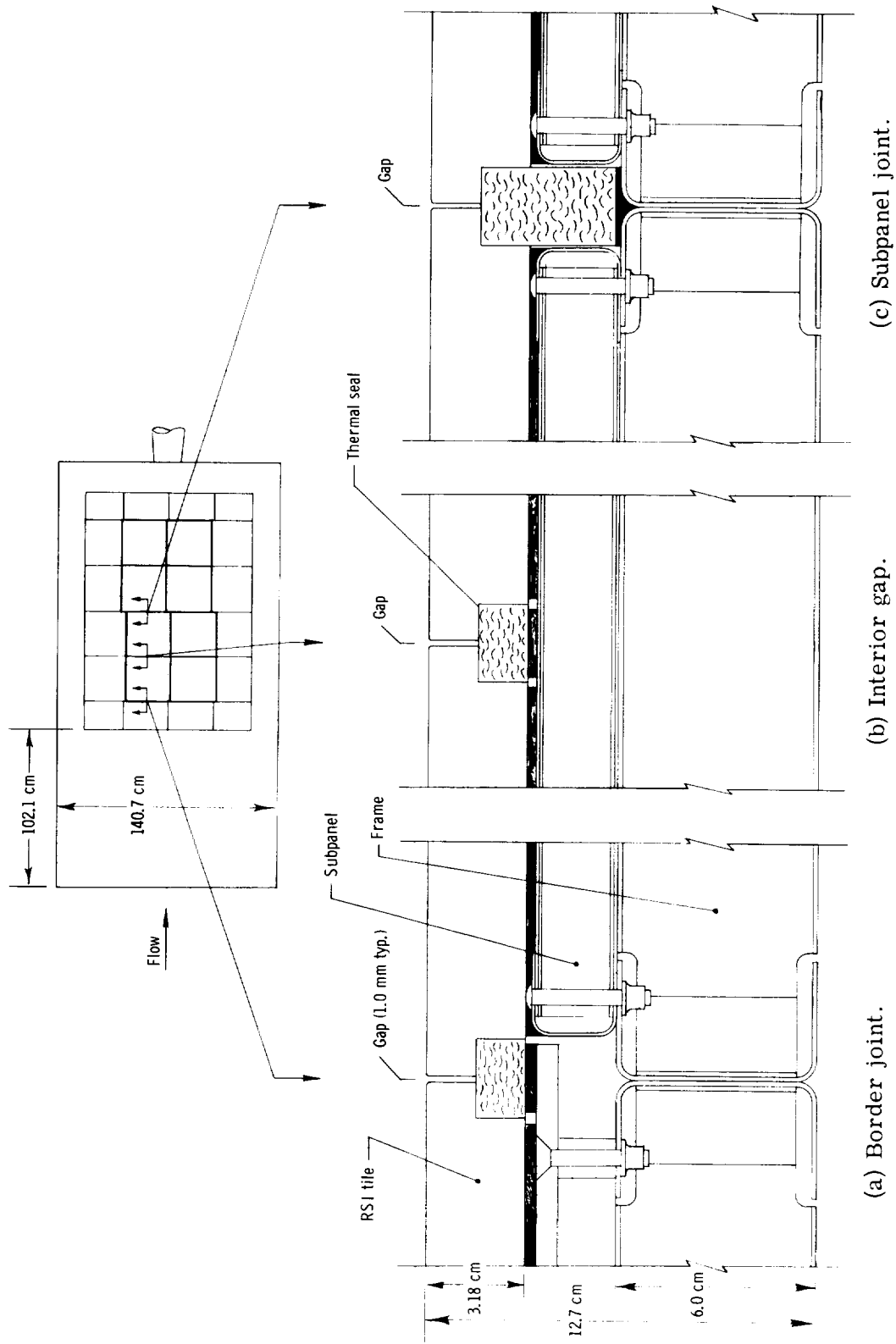
(c) Subpanel joint.

Figure 5.- Cross section of panel tiles and joints.

34

L-76-105

Figure 6.- RSI test panel installed in panel holder of Langley 8-foot high-temperature structures tunnel.
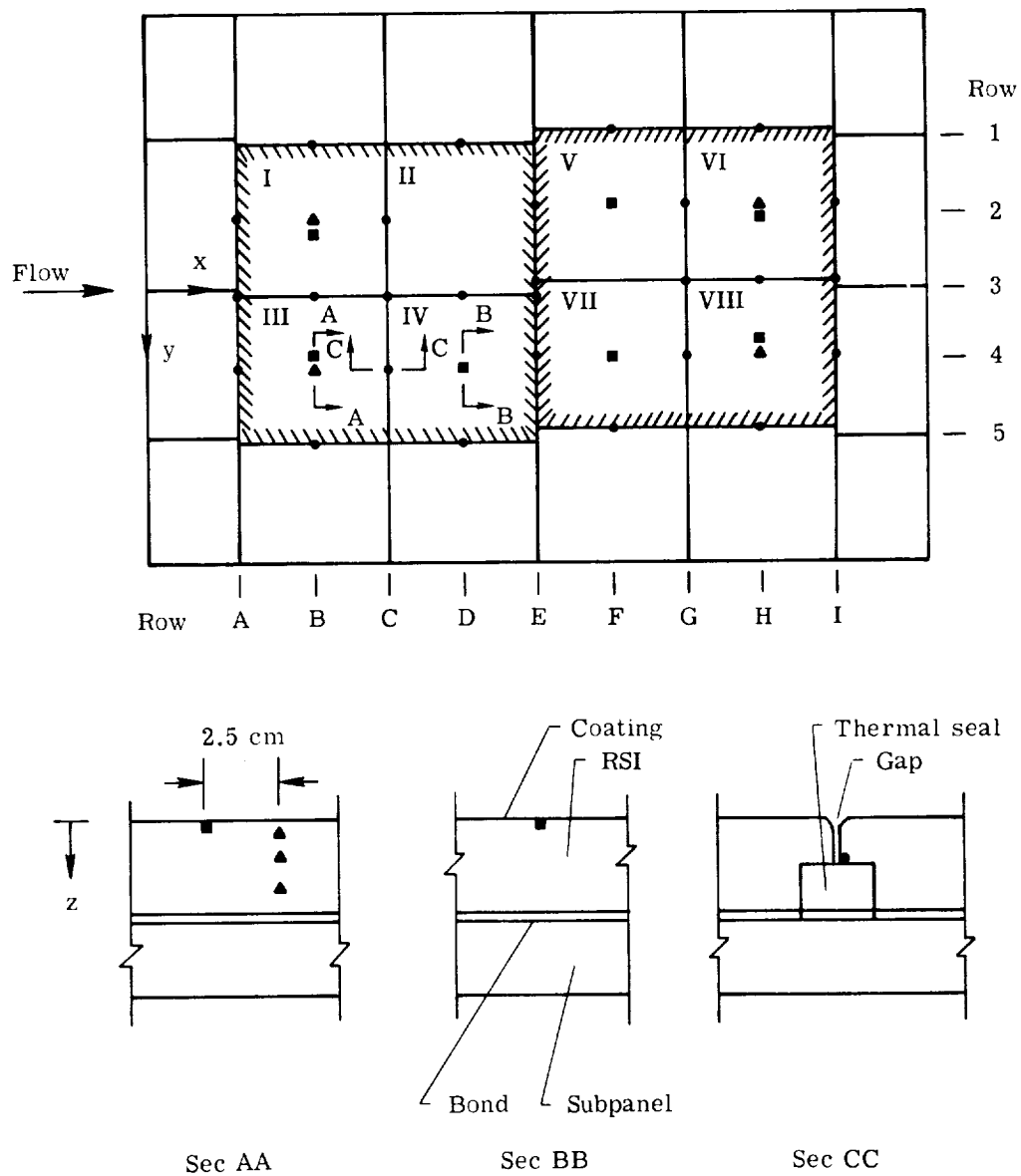
(a) LI-1542.

Figure 7.- Test panel with thermocouple locations indicated.

Front subpanel   Rear subpanel

Row

1

Flow →

A   A

3

5

Row   A   C   E   G   I

Subpanel

Frame

Base plate

Sec AA
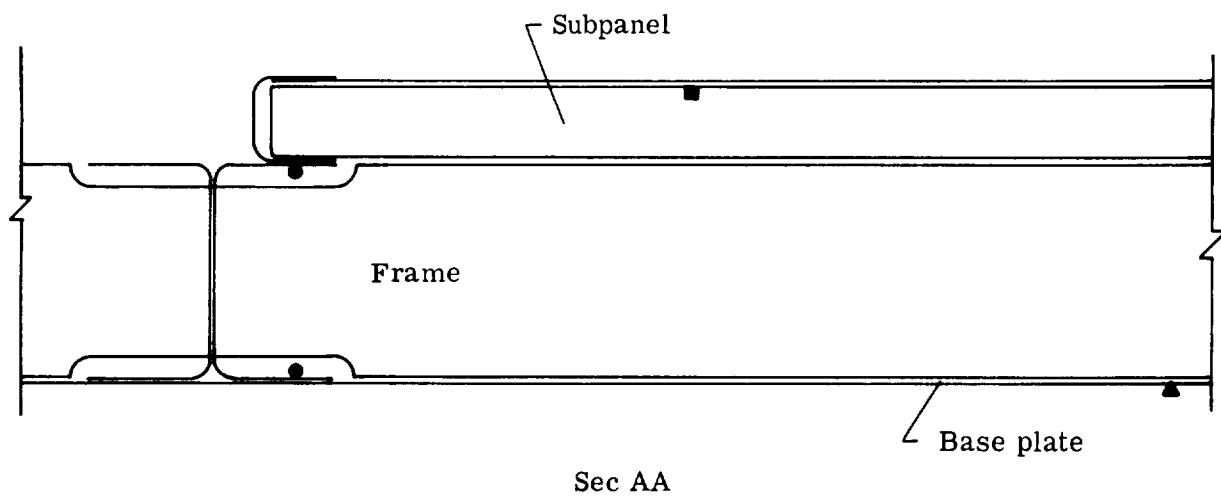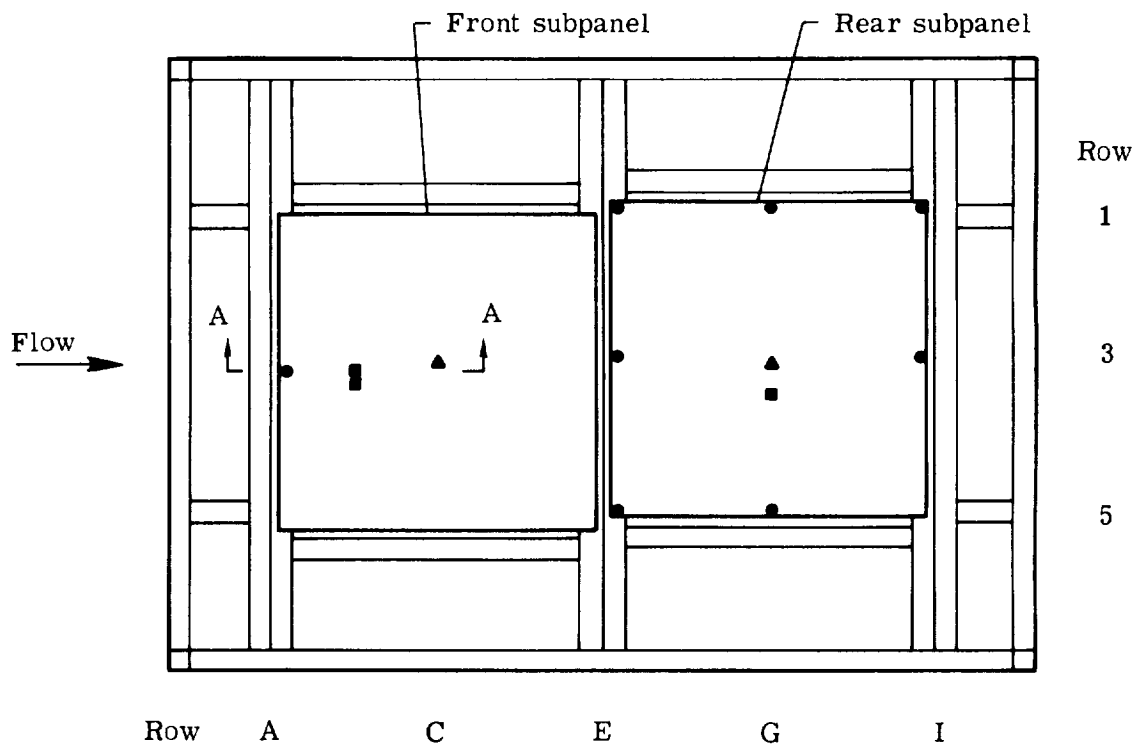
(b) Subpanels and support frame.

Figure 7.- Concluded.

37

Flow

Side view

TC plug   Surface TC

Rear view

Lead strip

RSI coating

z, cm
0

0.51

1.27

2.29

Surface TC

(a) Rear view.

Apparent thermocouple
depth, 1 mm

(b) Side view.
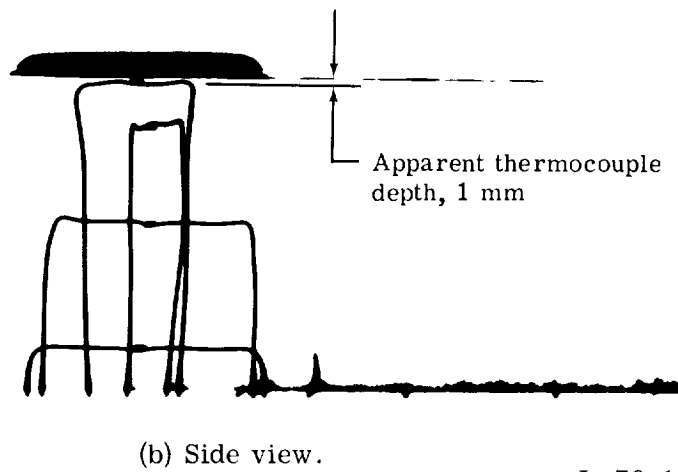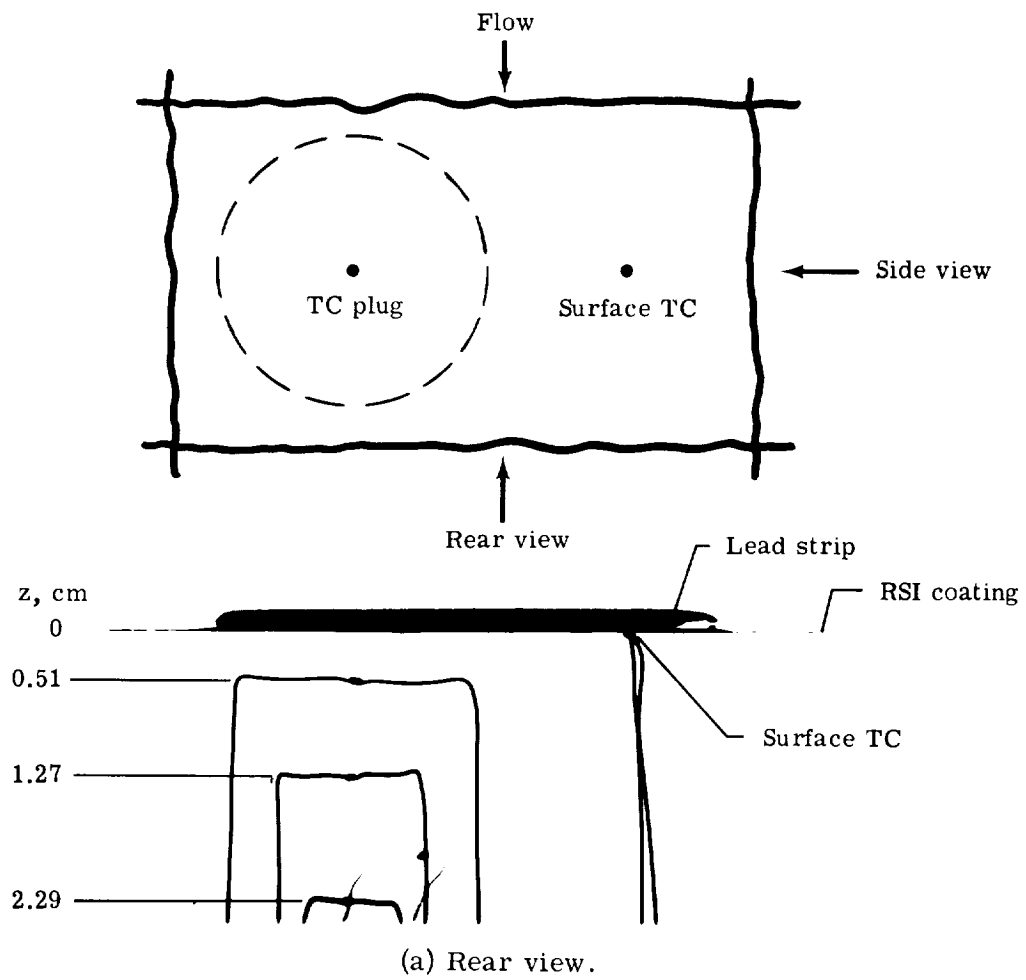
L-76-106

Figure 8.- X-ray photograph of thermocouple (TC) instrumentation.

38
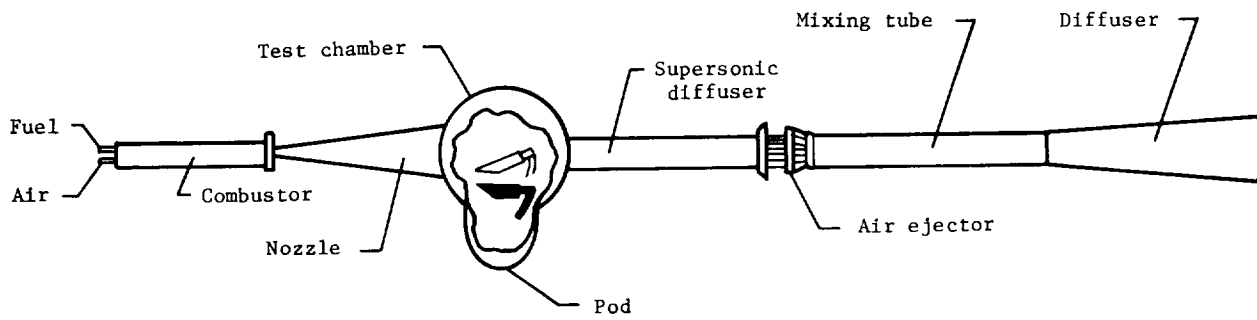
Figure 9.- Langley 8-foot high-temperature structures tunnel.
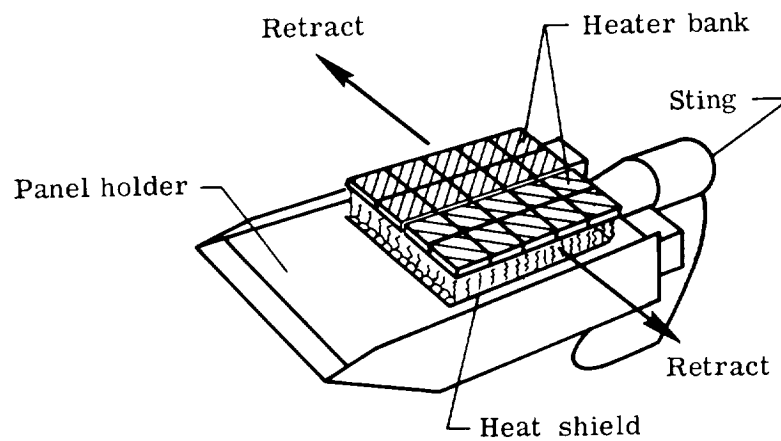
(a) Radiant heaters without acoustic covers.
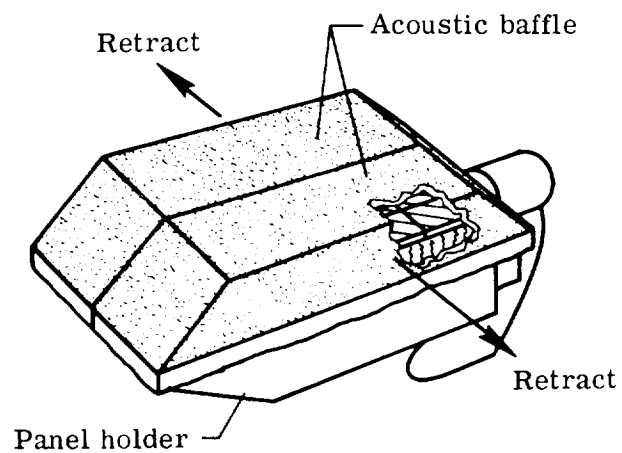
(b) Radiant heaters with acoustic covers.

Figure 10.- Retractable radiant heaters with and without acoustic covers.
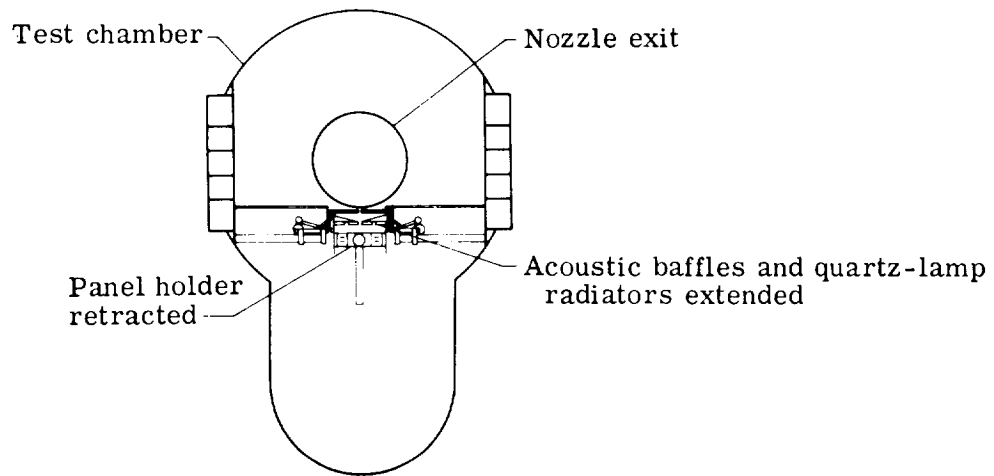
(a) Pretest and posttest.
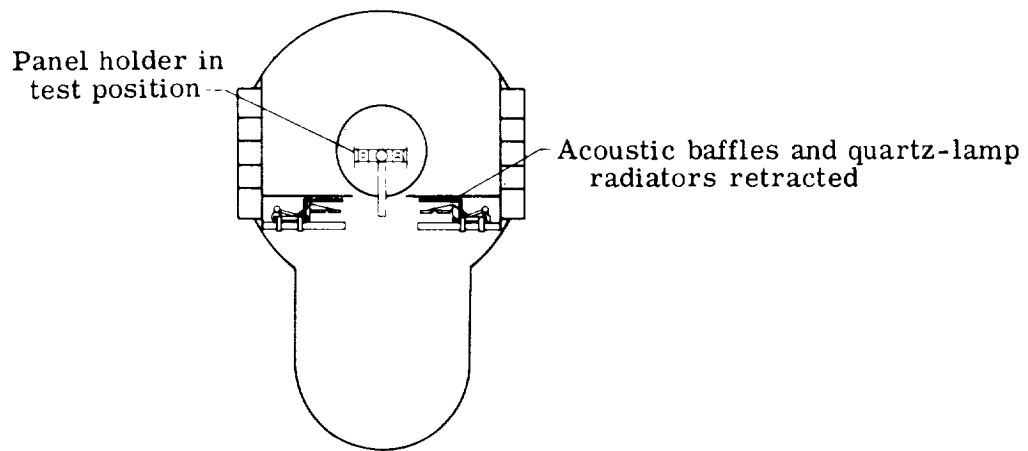
(b) During test.

Figure 11.- Cross-sectional views of test section.
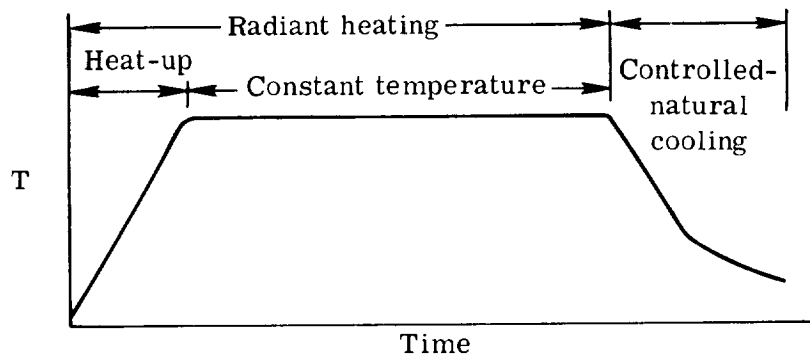
(a) Radiant heating (mode I).
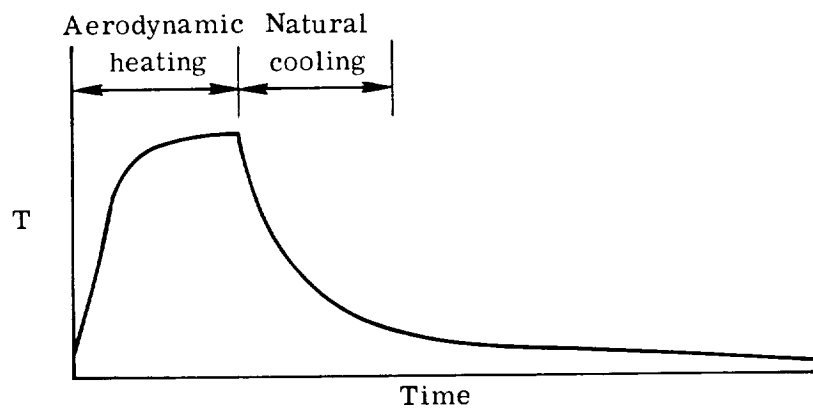
(b) Aerodynamic heating (mode II).
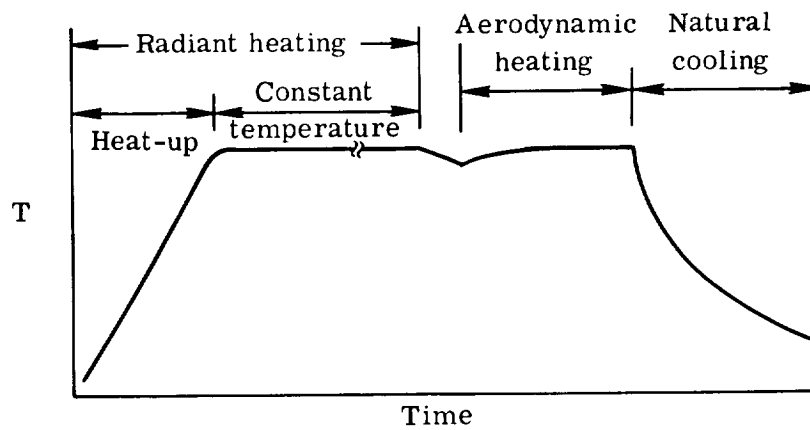
(c) Radiant heating and aerodynamic heating (mode III).

Figure 12.- Typical surface temperature histories.

41
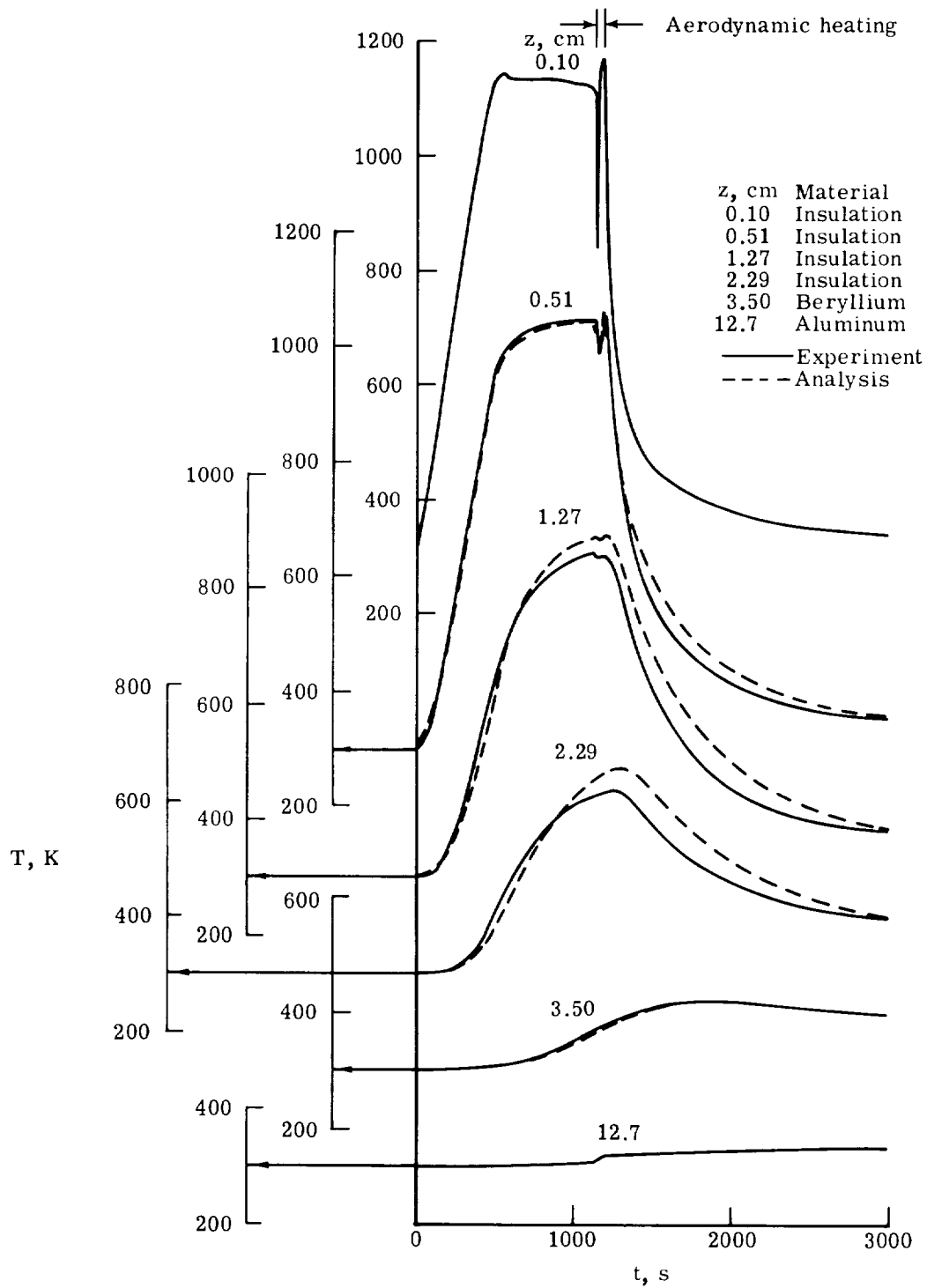
(a) Entry cycle.

Figure 13.- Temperature history for mode III test (test 10).
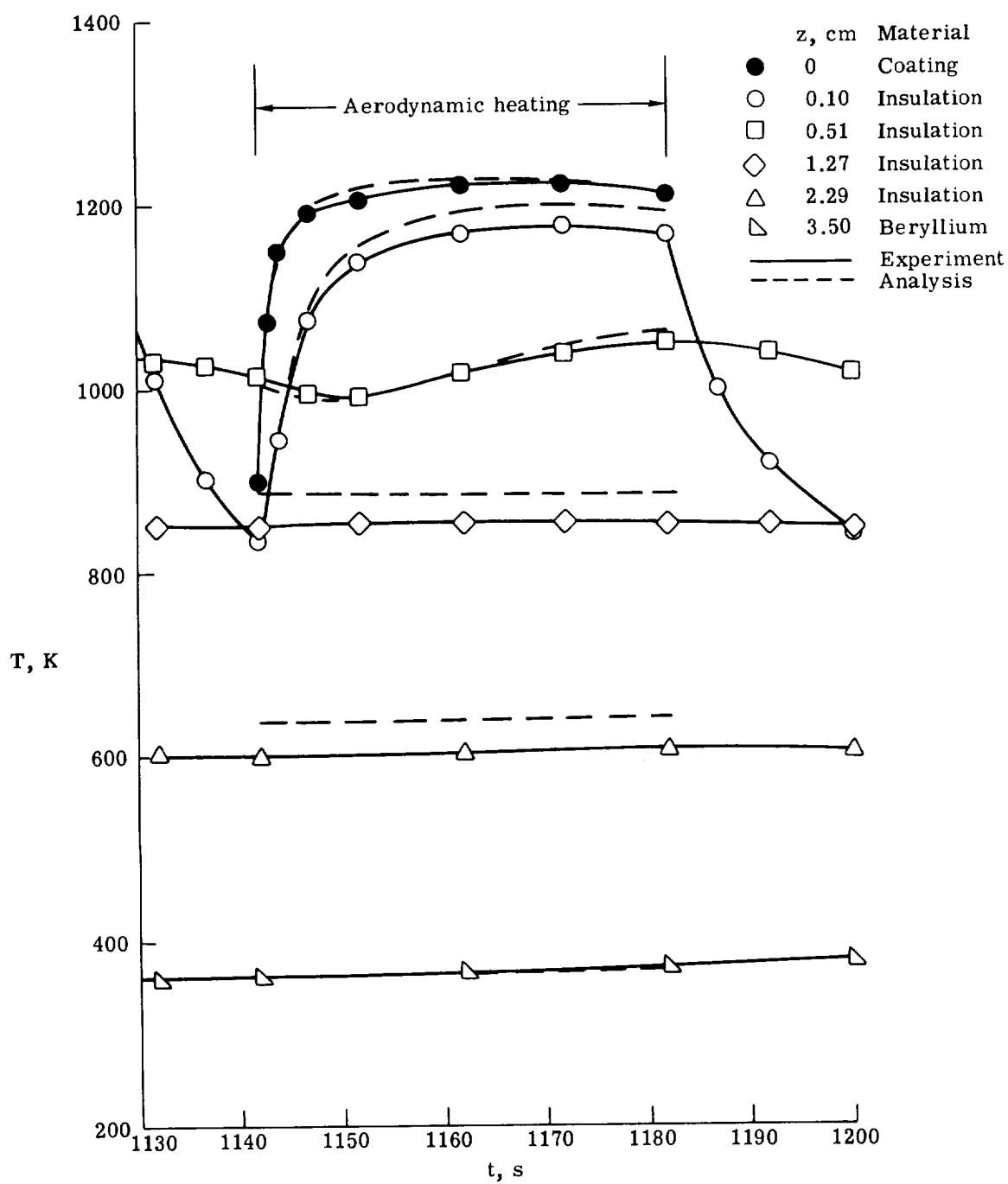
(b) Aerodynamic heating phase.

Figure 13.- Concluded.
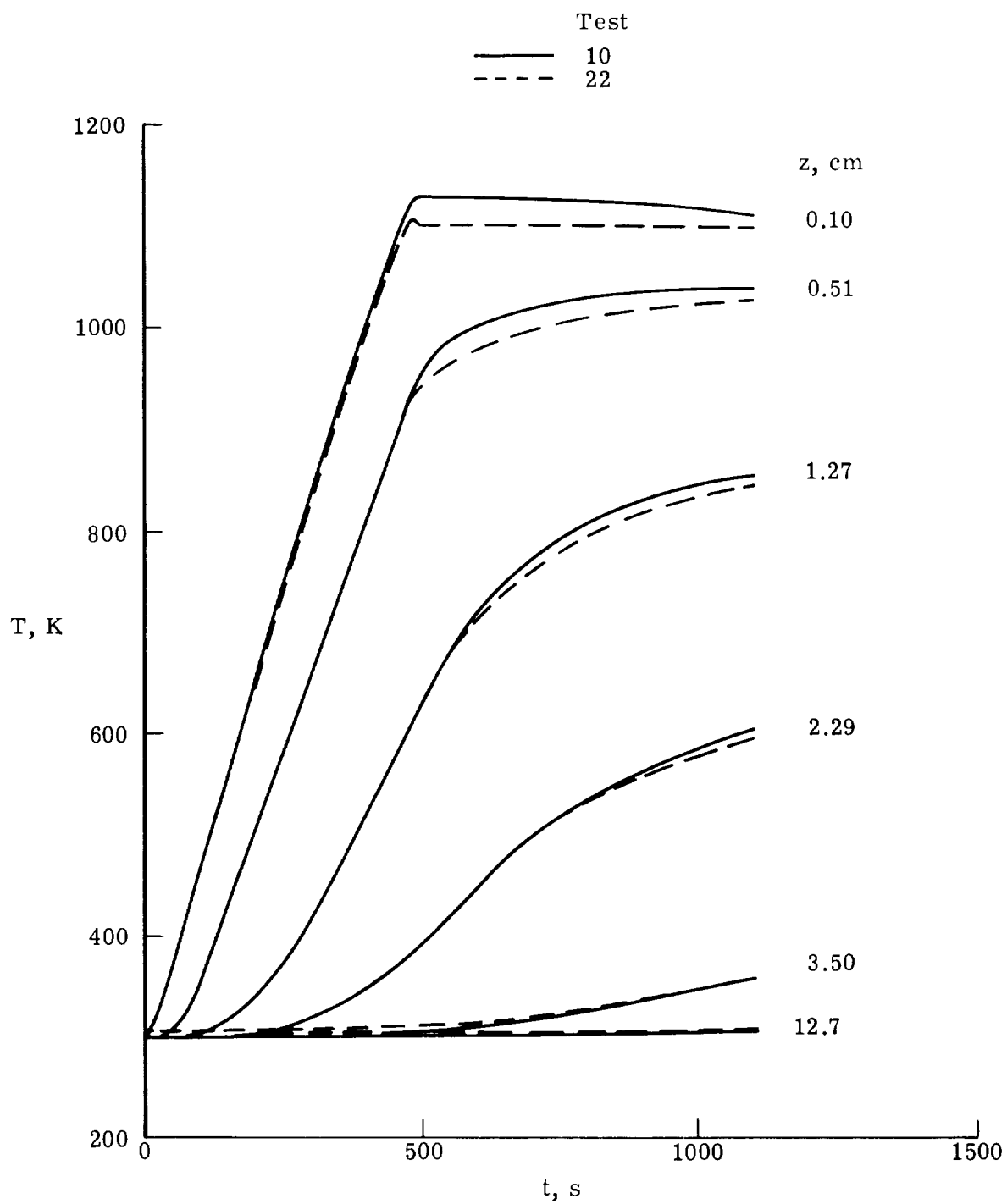
Figure 14.- Effect of repetitive thermal cycles on panel temperature histories.

Flow

Row

A

C

E

G

I

Row   5   3   1

L-76-107
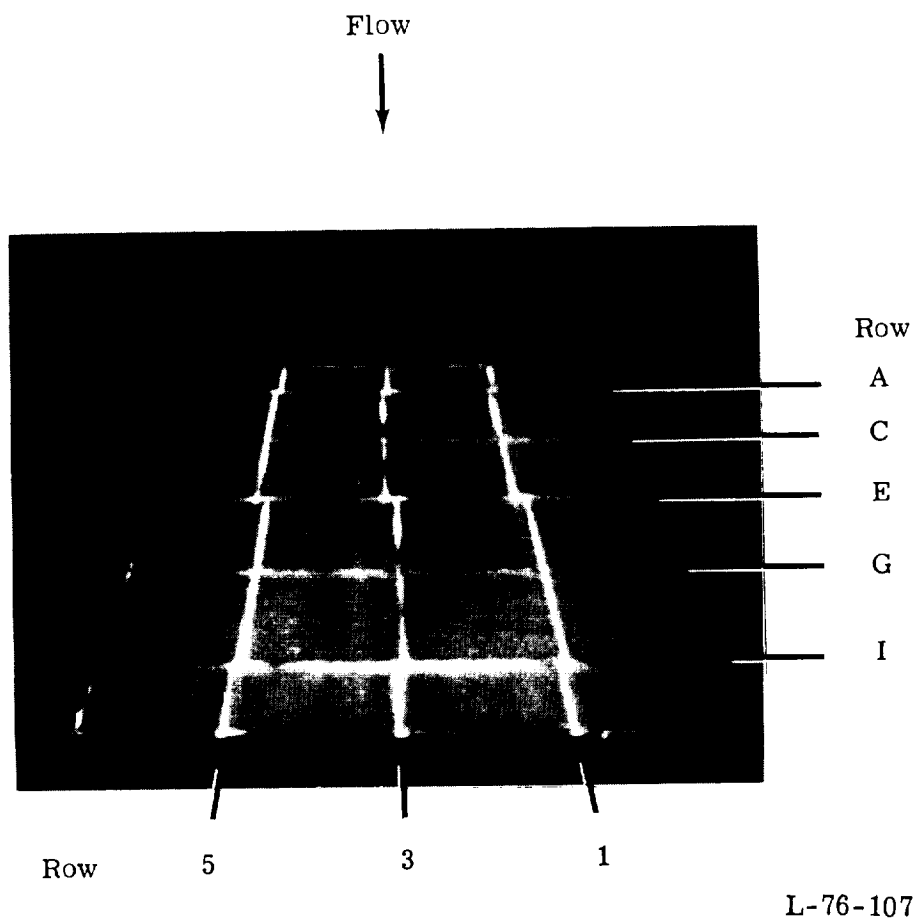
(a) Visible glow.

Figure 15.- Hot panel during aerodynamic heating of mode III test (test 10).

45
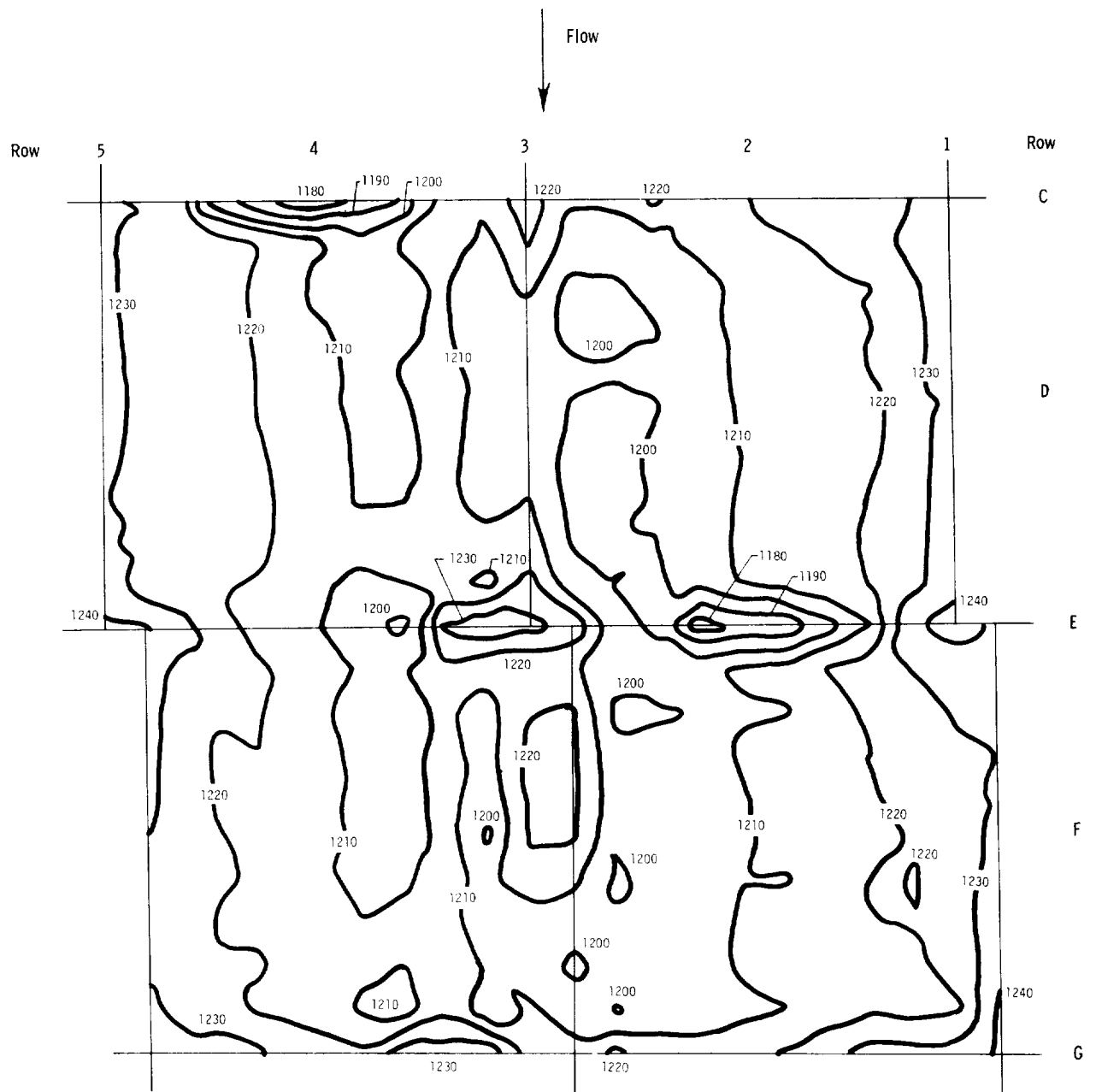
(b) Isothermal plot (temperature in K).

Figure 15.- Concluded.
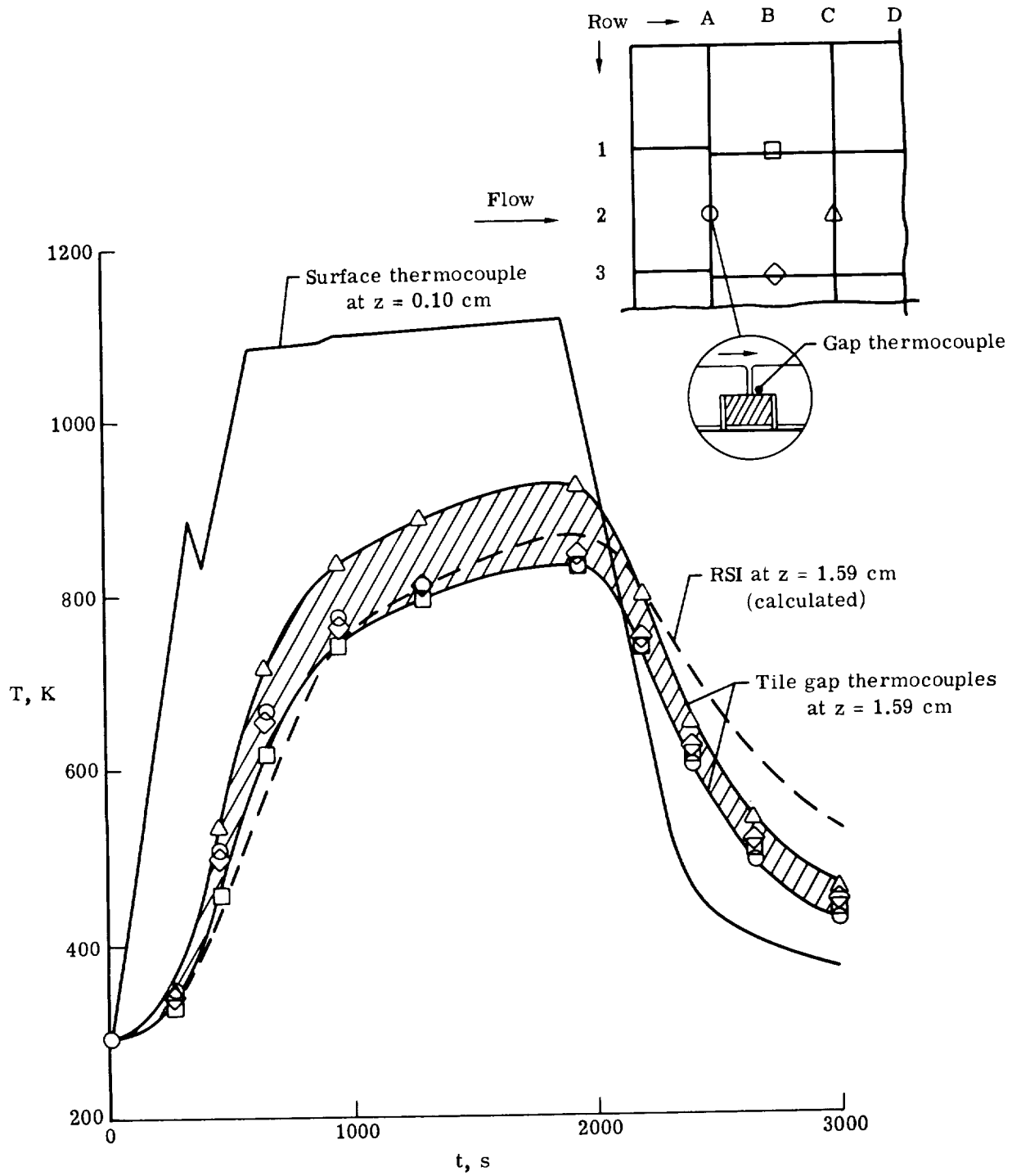
Figure 16.- Temperature history of gap around tile I for mode I test (test 13).
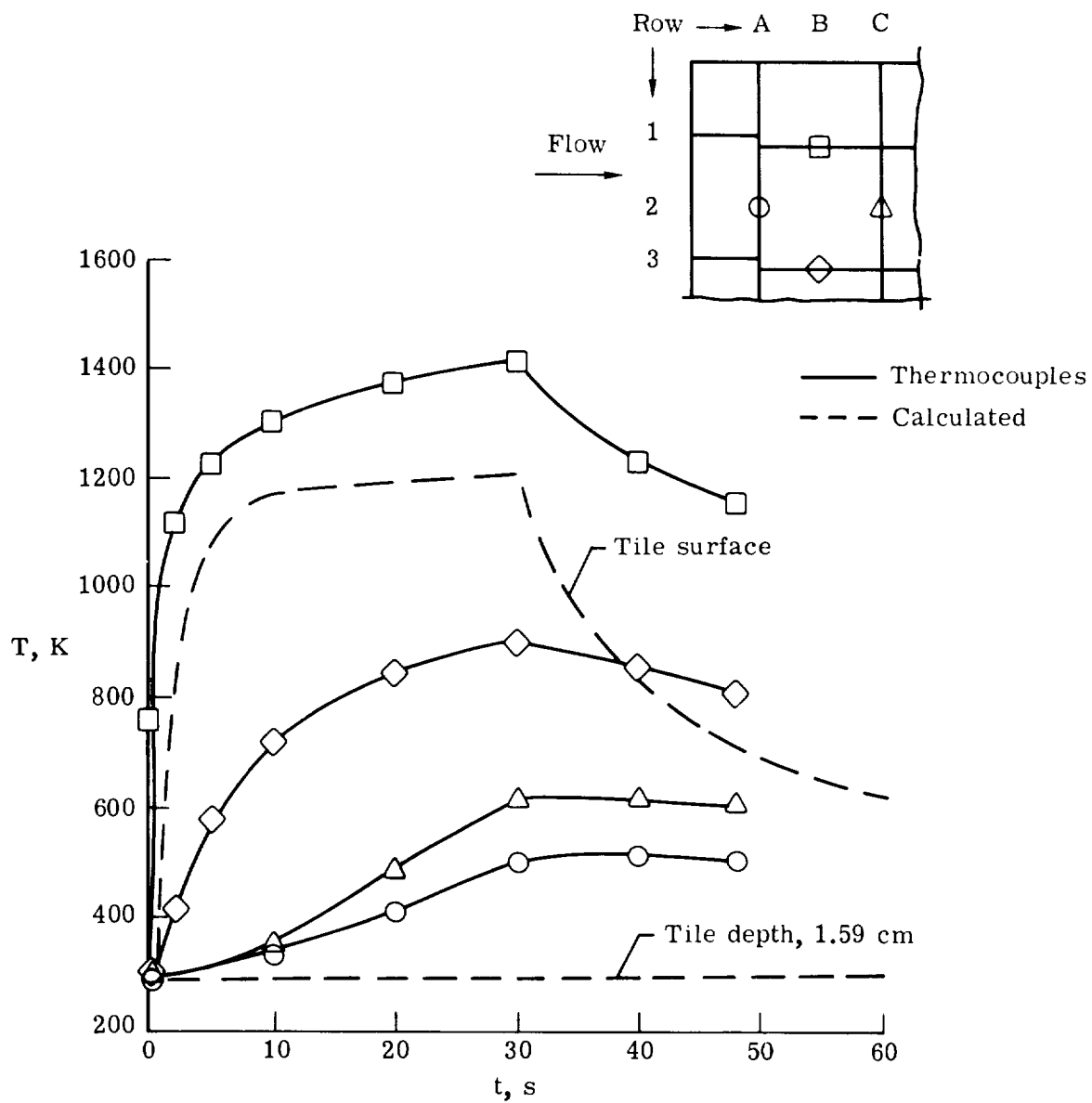
Figure 17.- Gap temperature histories of tile I for mode II test (test 5).
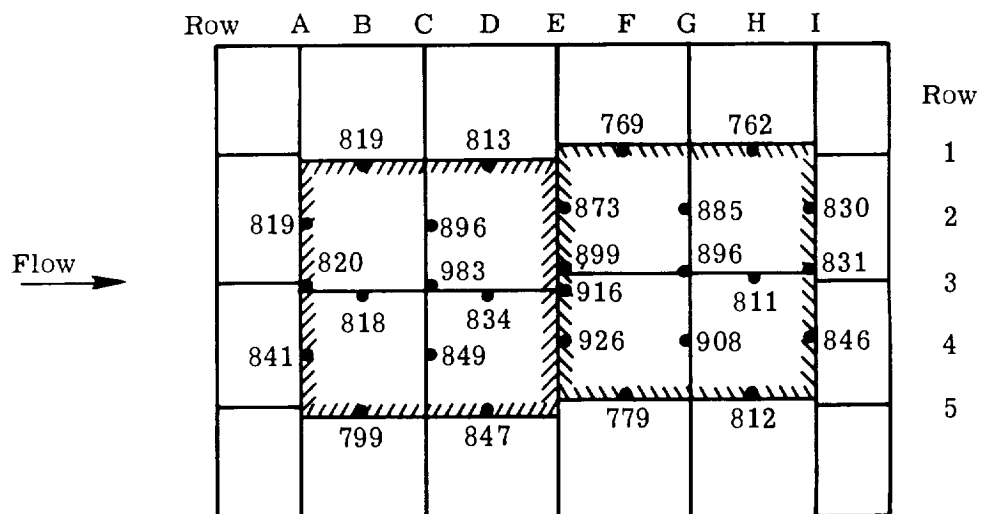
(a) Radiant heating (t ≈ 1100 s; surface temperature of 1100 K).
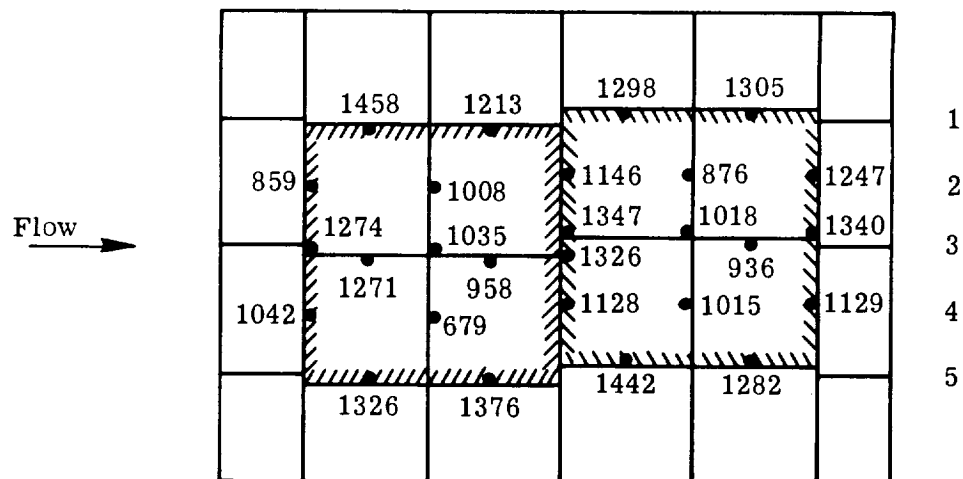
(b) Aerodynamic heating (t = 1215 s; surface temperature of 1180 K).

Figure 18.- Typical temperature (K) at z = 1.59 cm for mode III test (test 8).
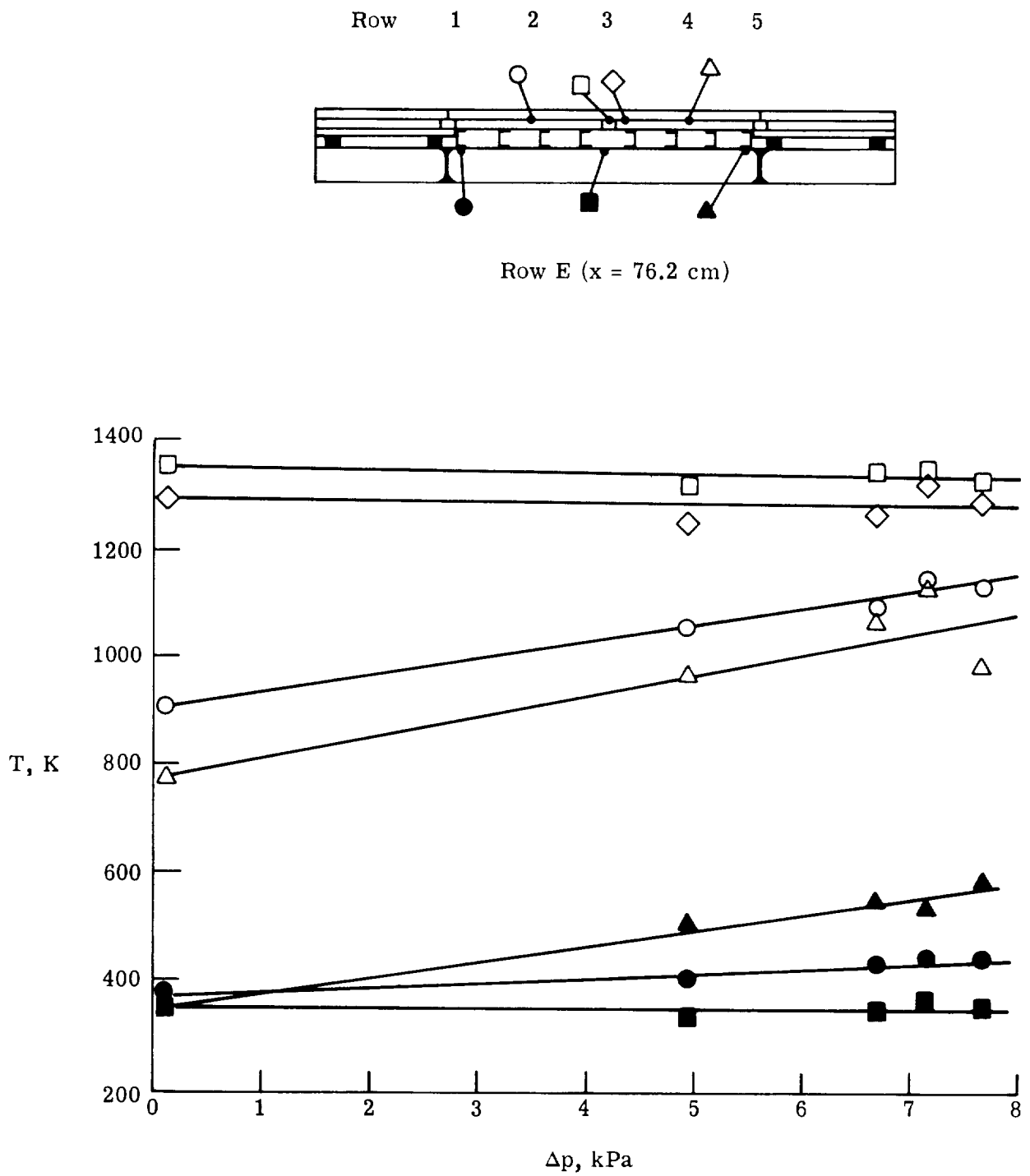
Figure 19.- Effects of differential pressure on panel temperature at row E
(mode III tests).
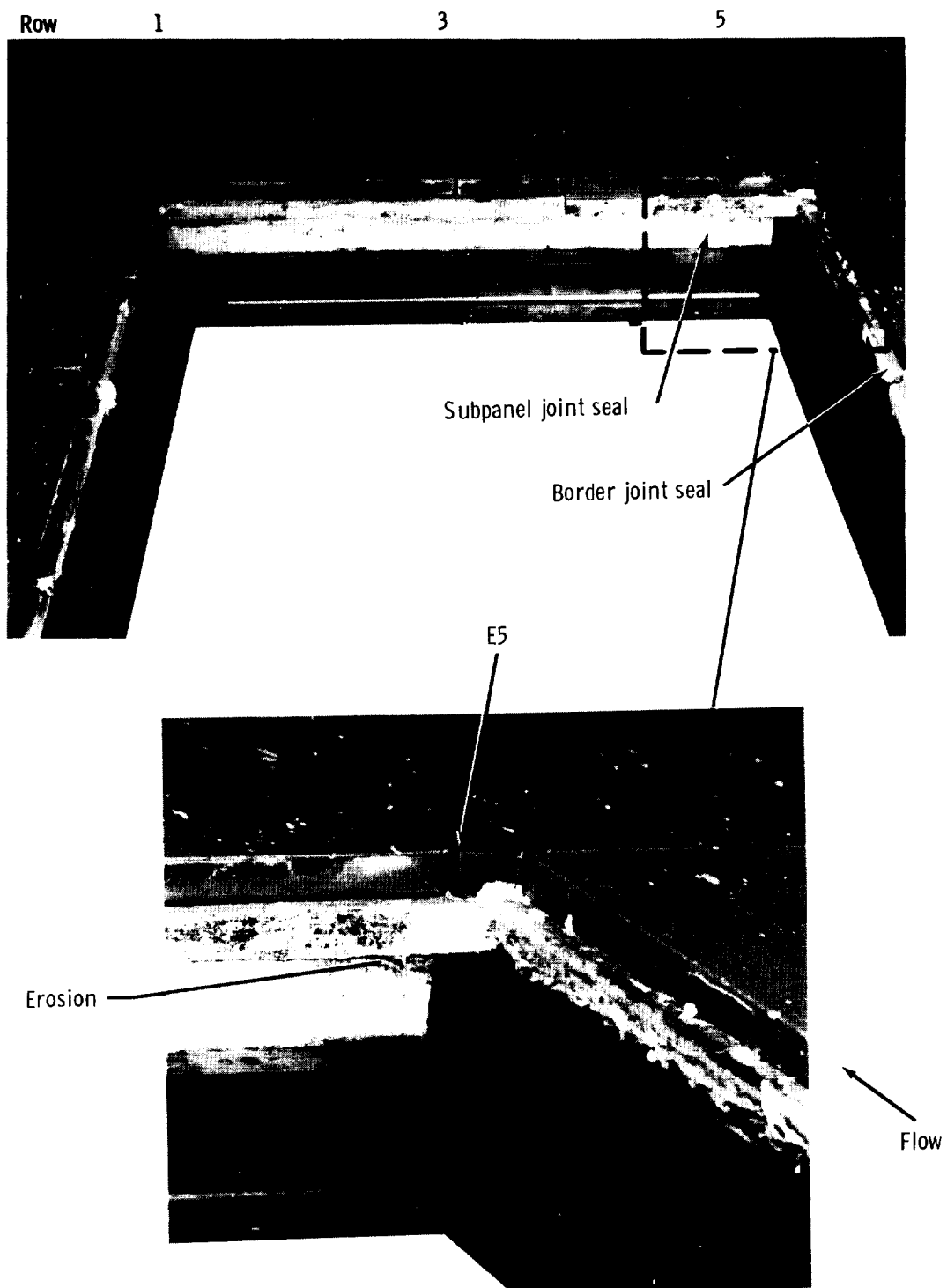
Figure 20.- Thermal seals of subpanel joint E5 at conclusion of tests.

Flow

L-76-109

Figure 21.- Appearance of tile surface at conclusion of tests.

4 mm

Flow
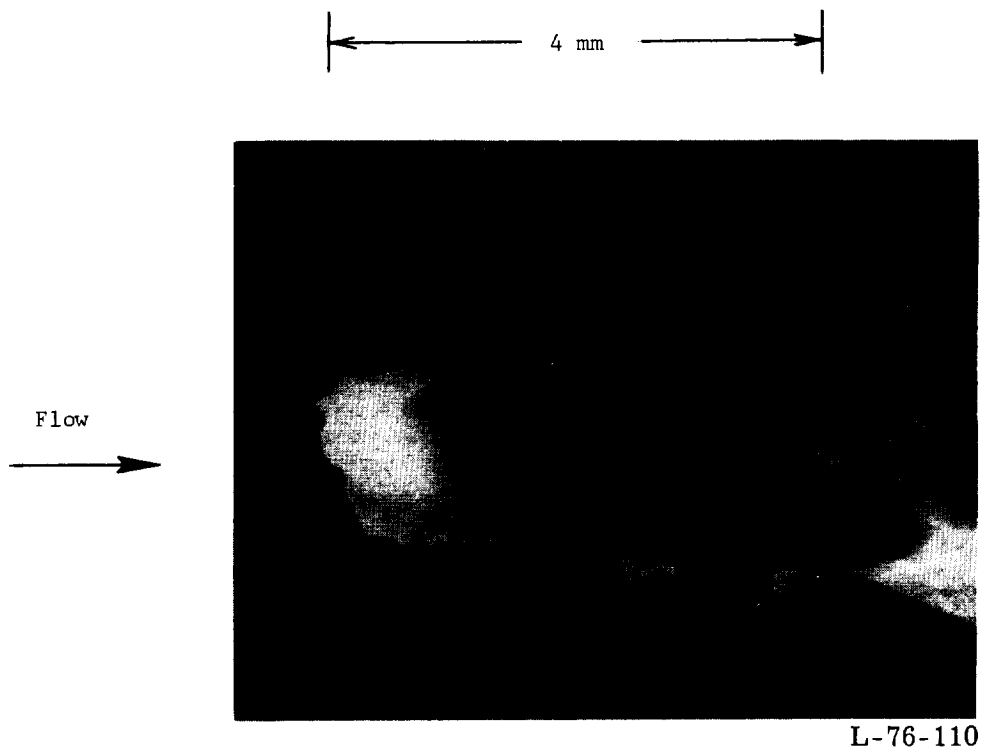
L-76-110

Figure 22.- Photomicrograph of impact crater (row I2).

Flow →
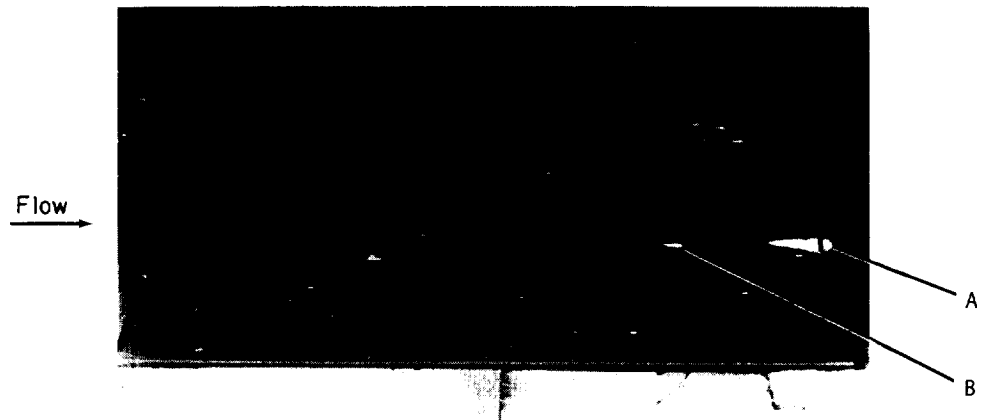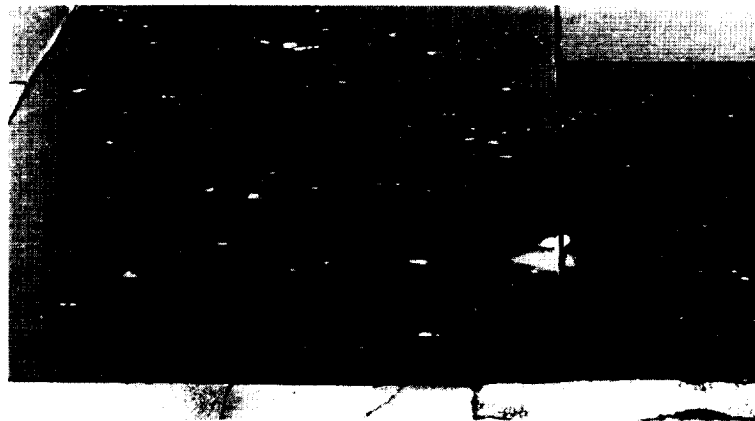
(a) Posttest 8.

(b) Posttest 12.

(c) Posttest 23.

L-76-111

Figure 23.- History of crater damage and repair.
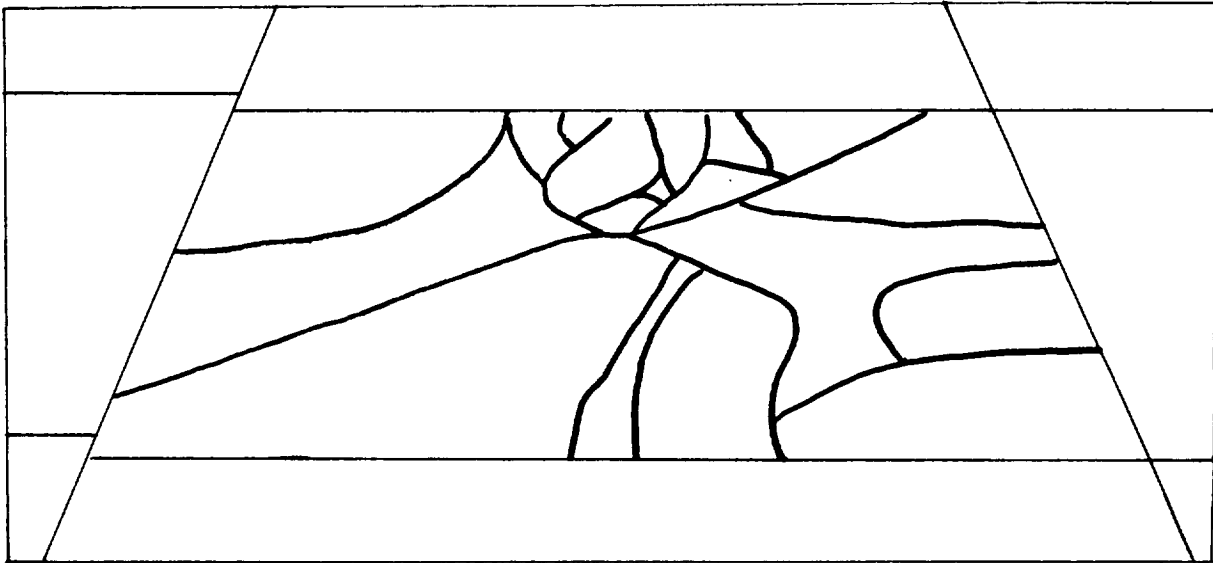
(a) Pretest 4.
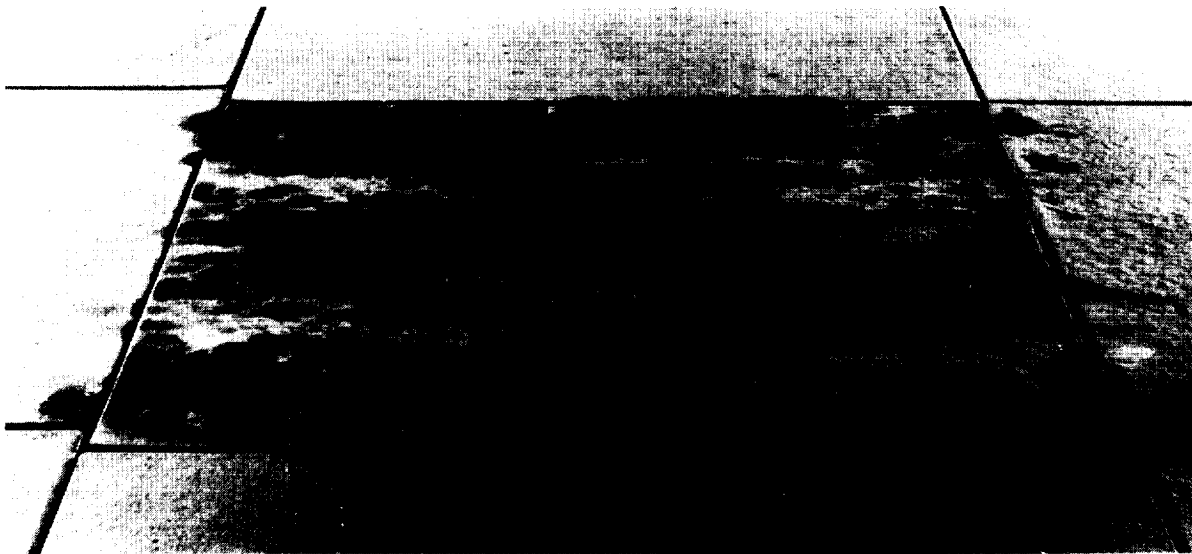
L-76-112

(b) Posttest 4.

Figure 24.- Crack patterns of tile coating (tile III).

8 mm

Flow →

Outer layer
of coating

Inner layer
of coating

Insulation
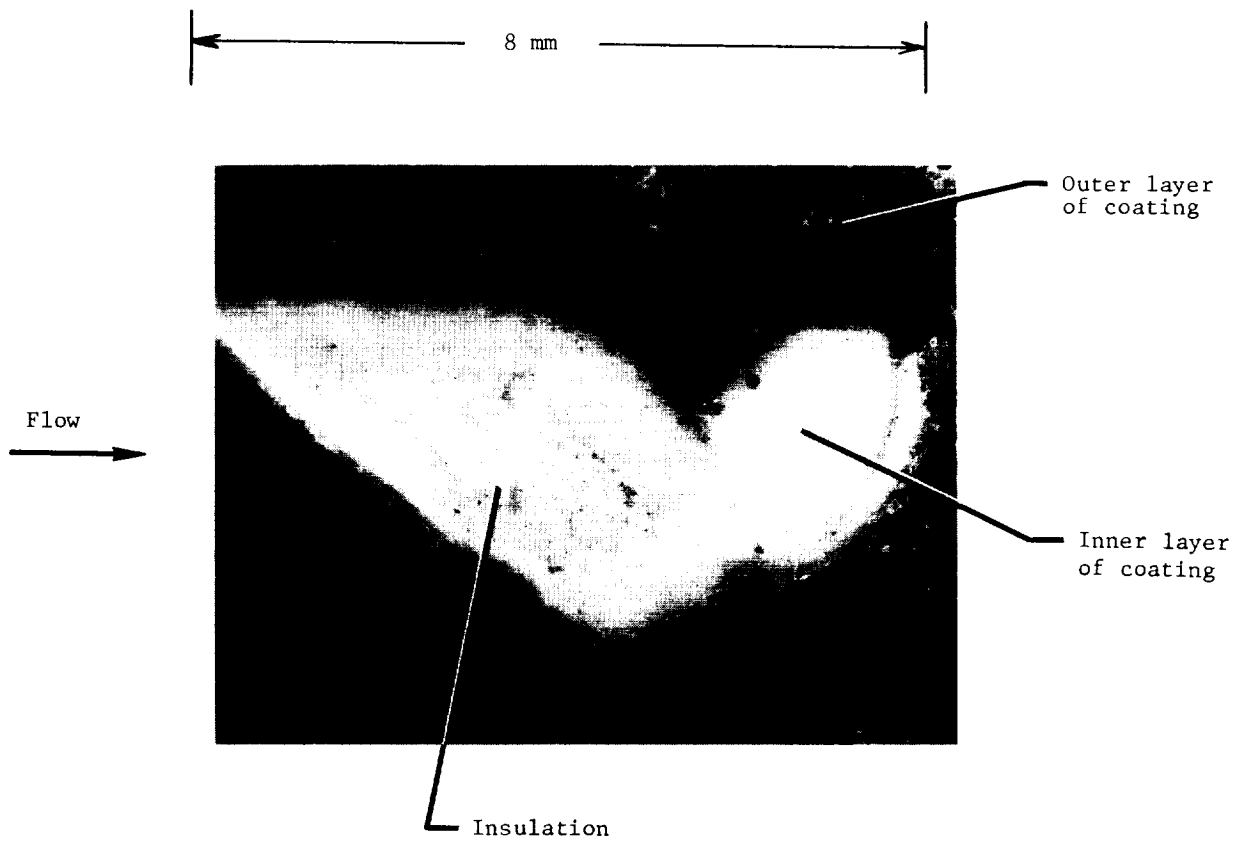
Figure 25.- Flaking damage to water-soaked tile.
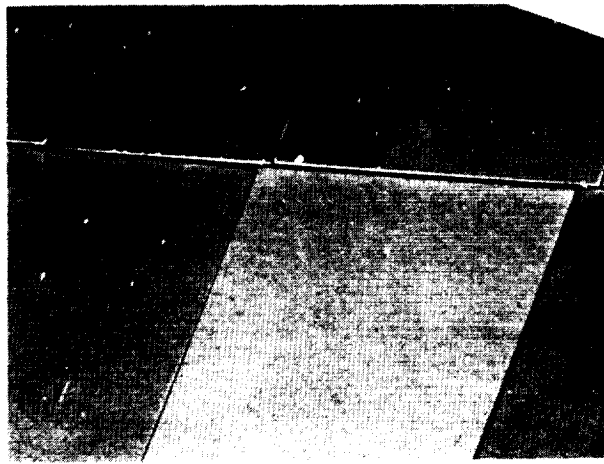
(a) Posttest 4.
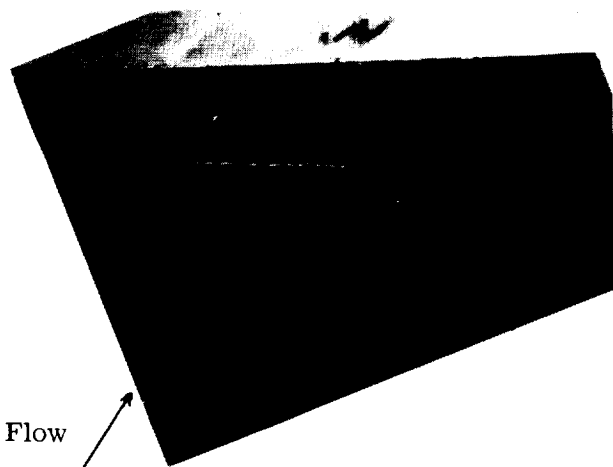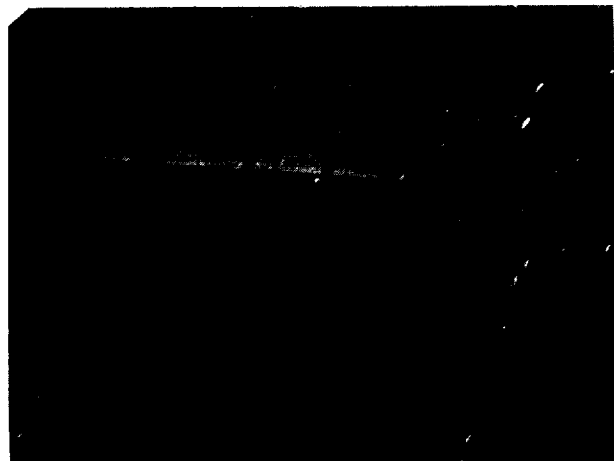
Flow

(b) Posttest 5.

(c) Posttest 23.

L-76-114

Figure 26.- Tile edge erosion of 0.4-mm forward-facing step along row I.

(a) A3.

(b) E3.
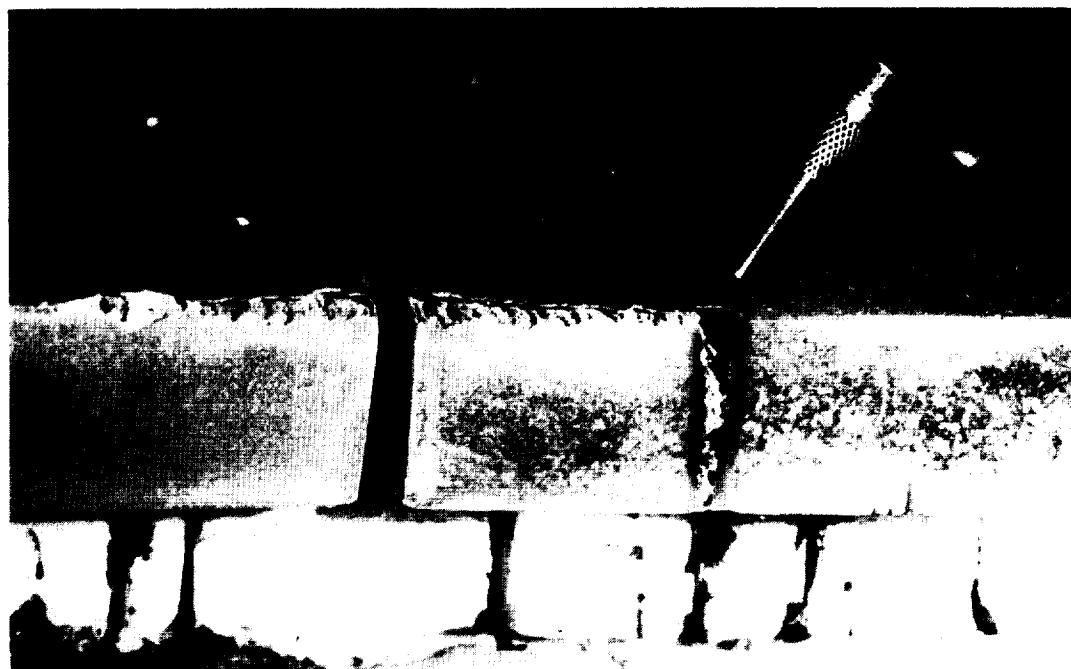
Figure 27.- Tile erosion from flow impingement at end of longitudinal gaps.
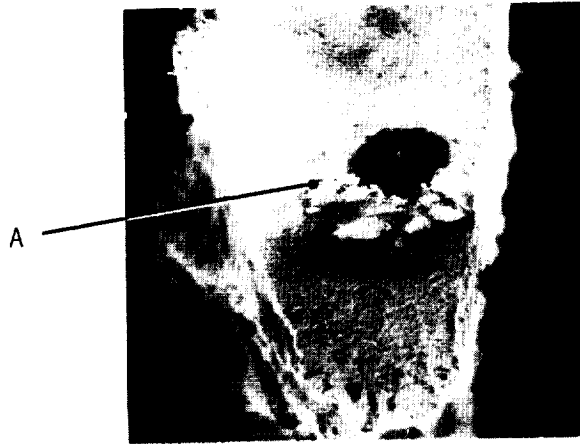
(a) Photomicrograph of erosion hole (×26).

(b) SEM of position A (×680).

(c) SEM of unexposed insulation (×680).

L-76-116

Figure 28.- Scanning electron micrograph (SEM) of erosion hole.

59
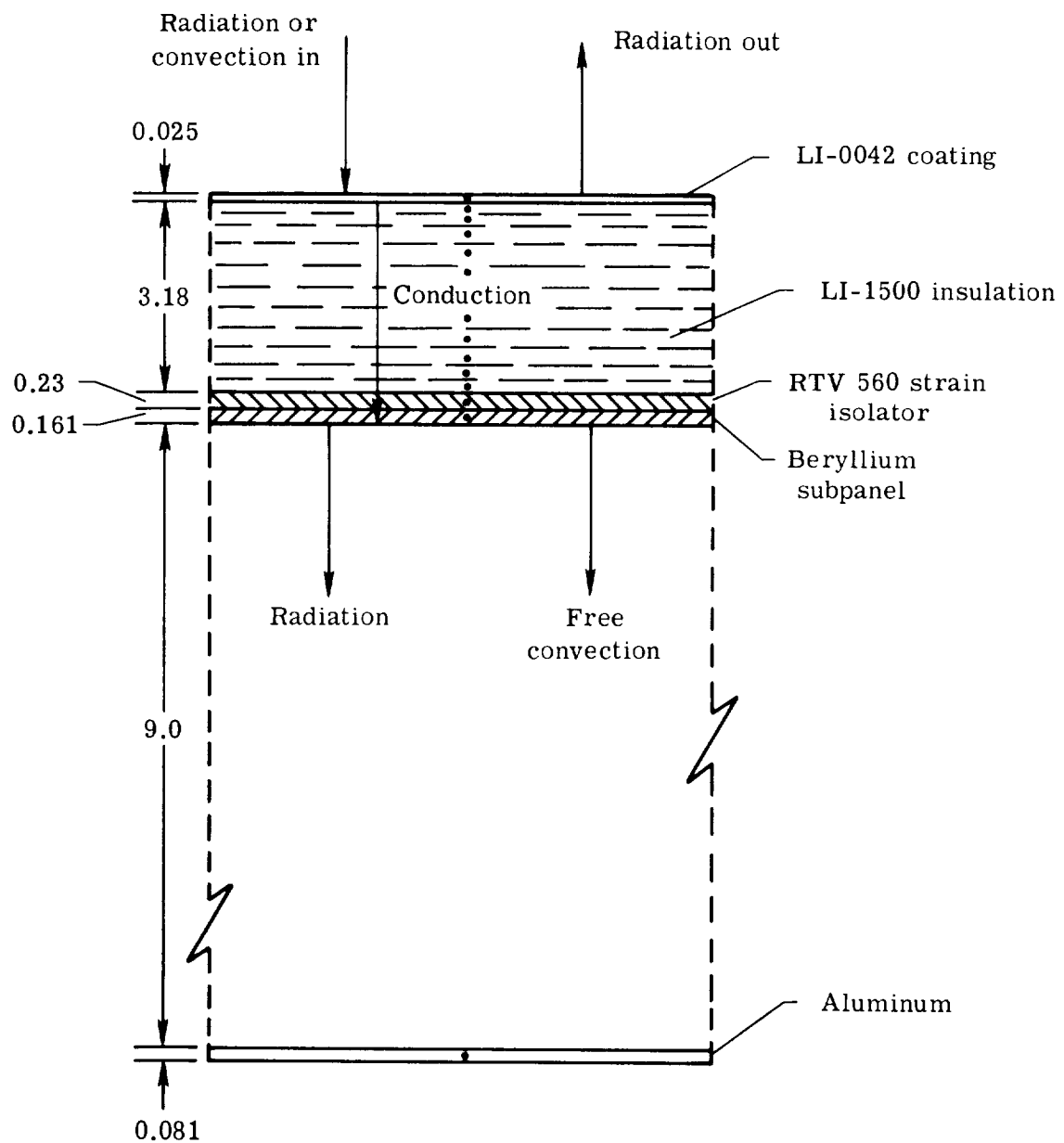
Figure 29.- Model of test panel used in thermal analysis.
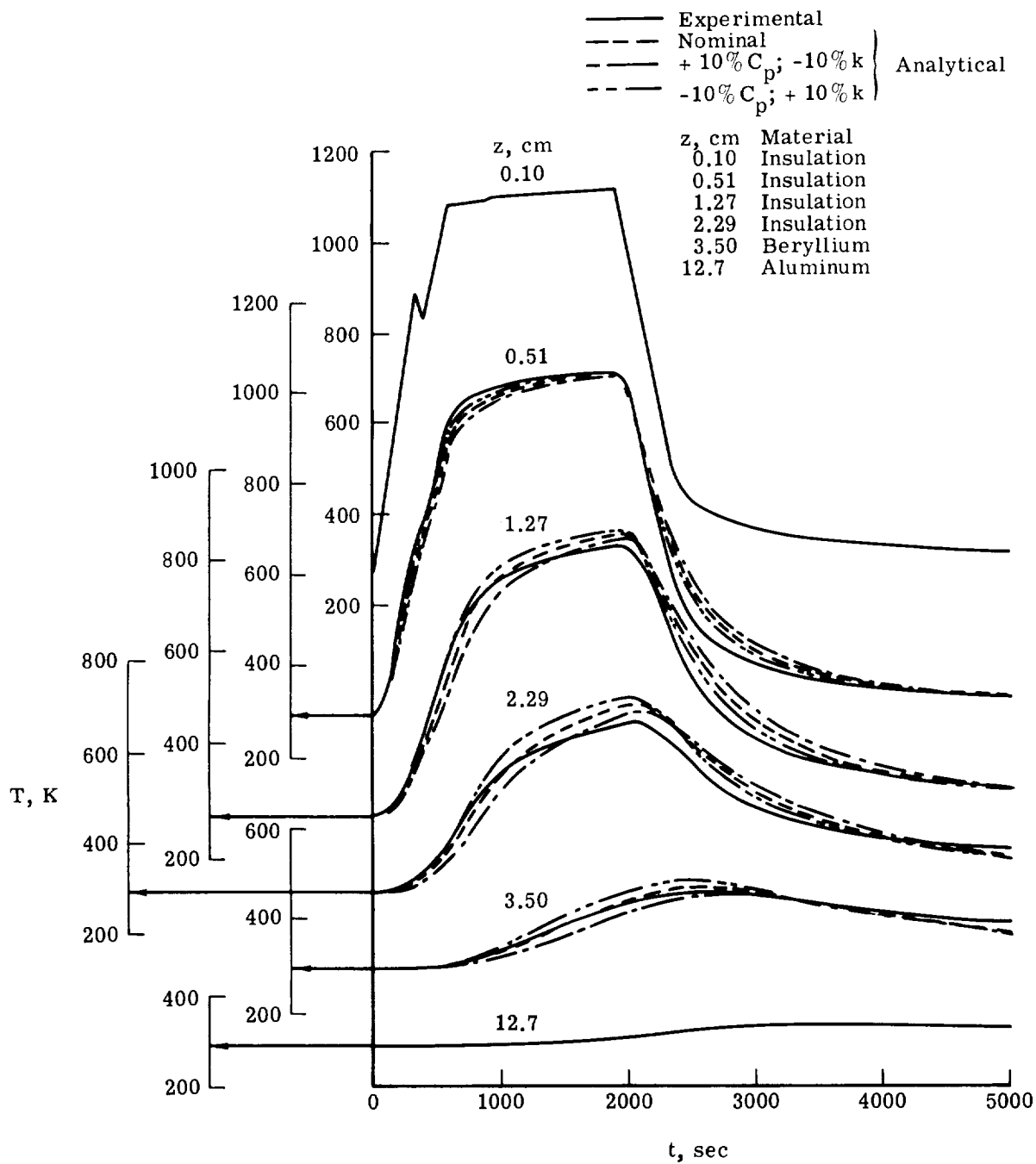
Figure 30.- Effect of thermal property variation on temperature histories of test panel.
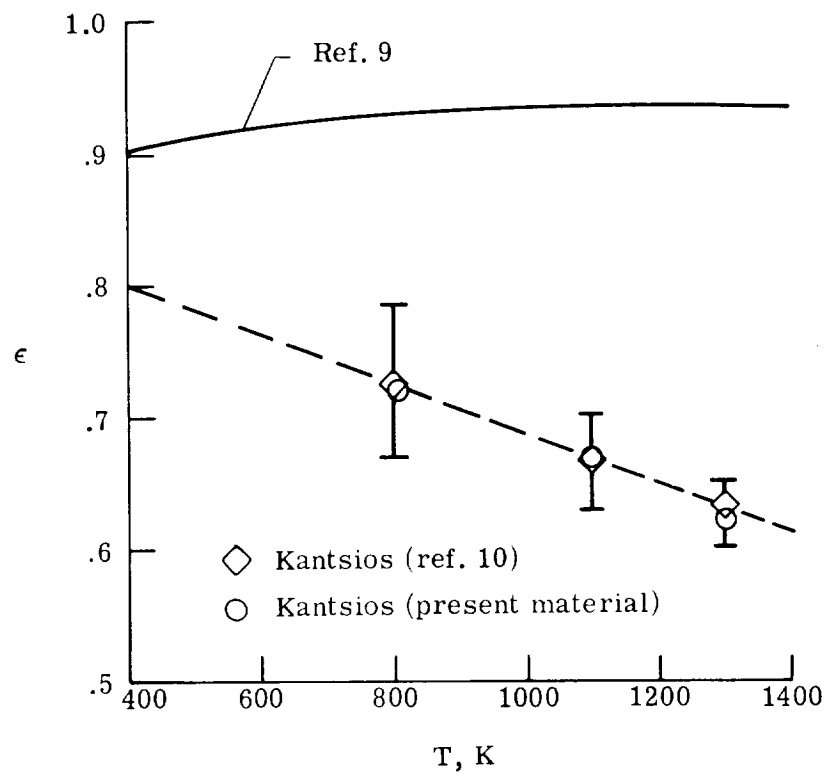
Figure 31.- Surface emissivity for LI-0042 coating.
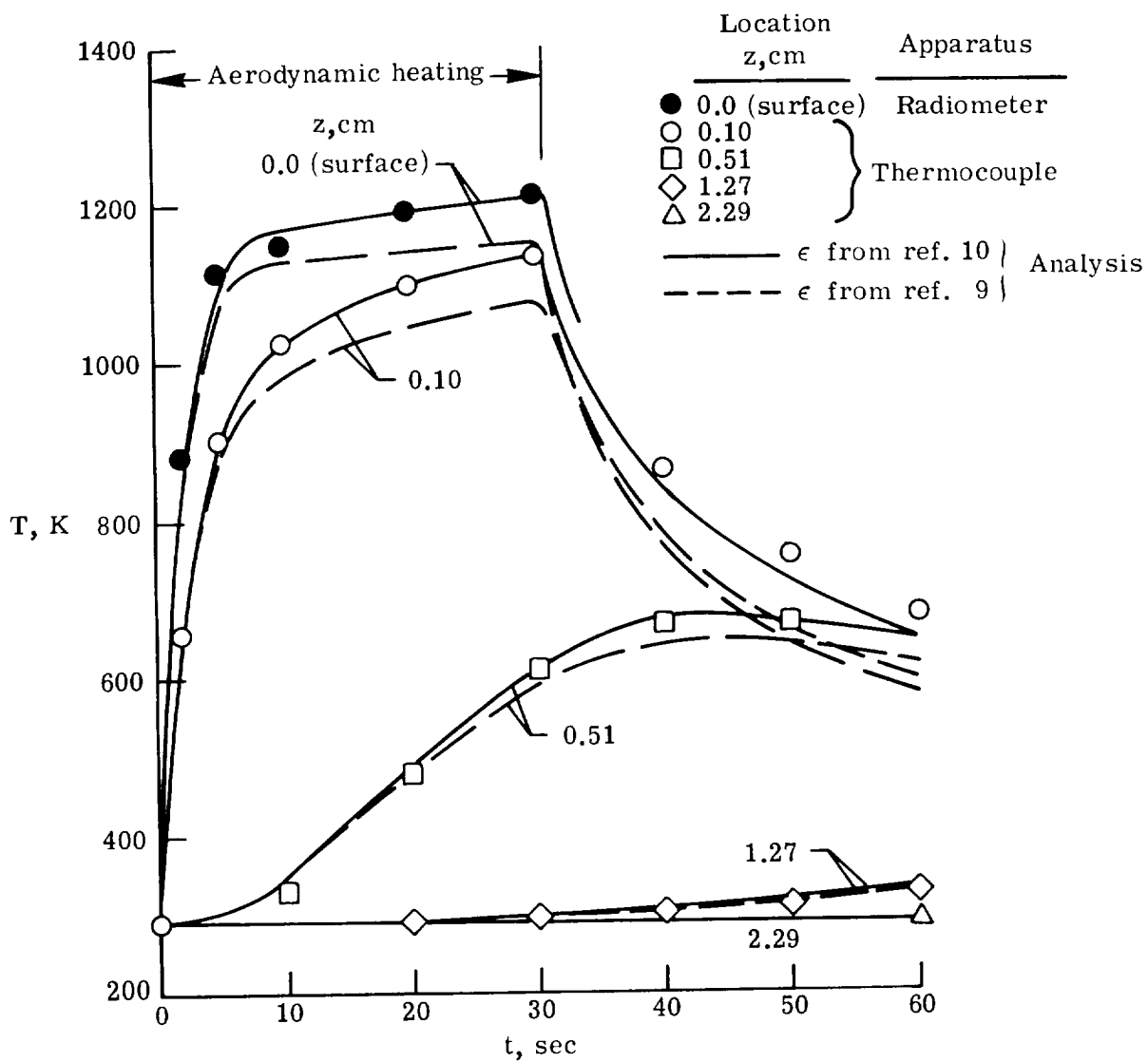
Figure 32.- Effect of surface emissivity on calculated temperature histories of test panel.
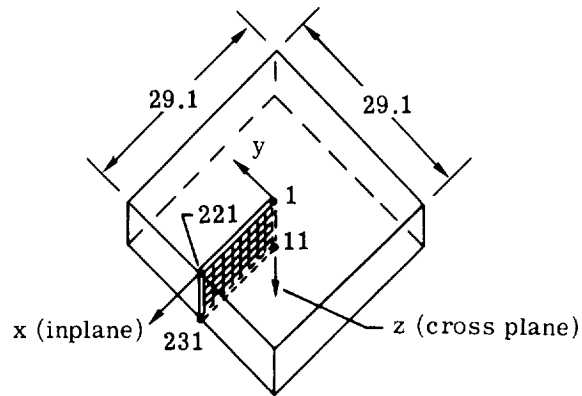
(a) Portion of tile modeled.
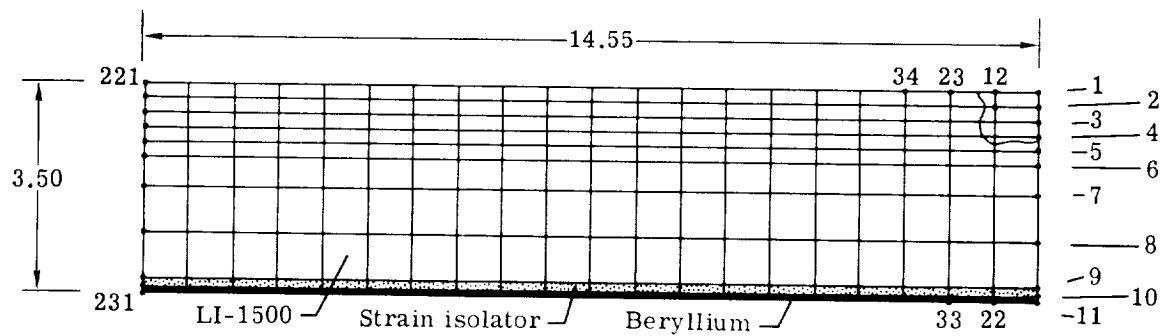
(b) Finite-element grid neglecting coating (all membrane elements).
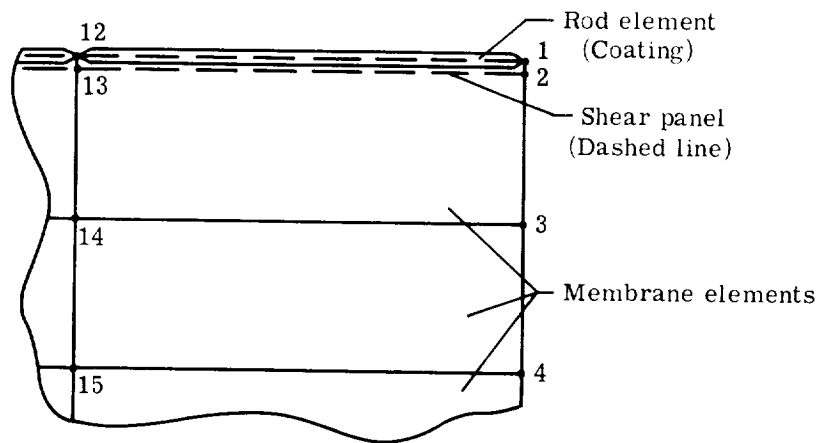
(c) Grid modified to include coating.

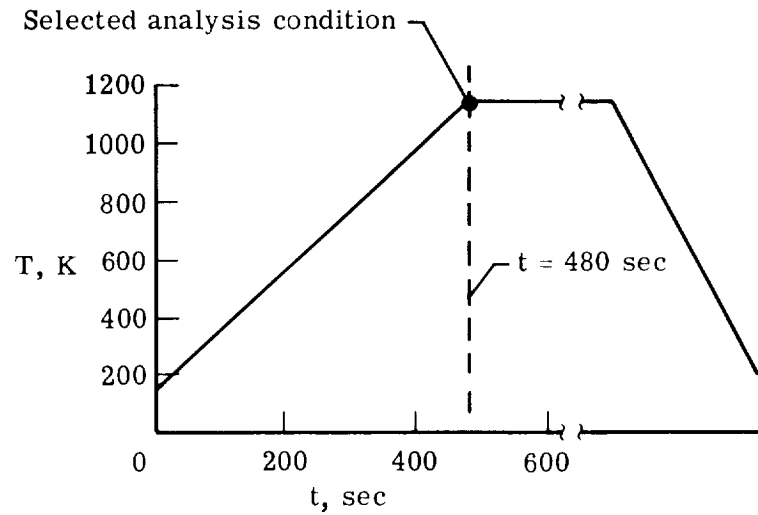Figure 33.- Finite-element model of LI-1542 tile. Dimensions are in centimeters, numbers by solid circles indicate joint numbers.
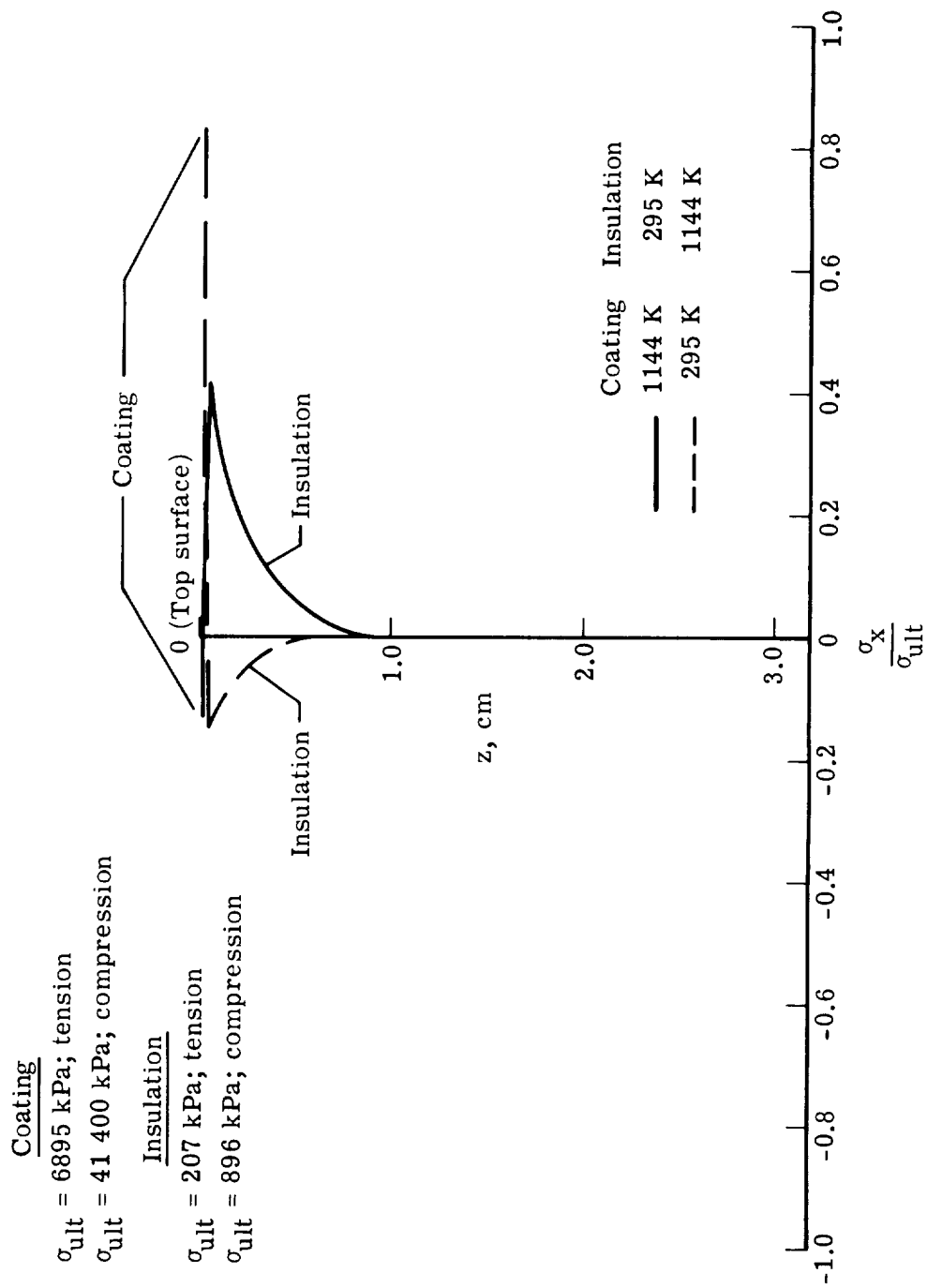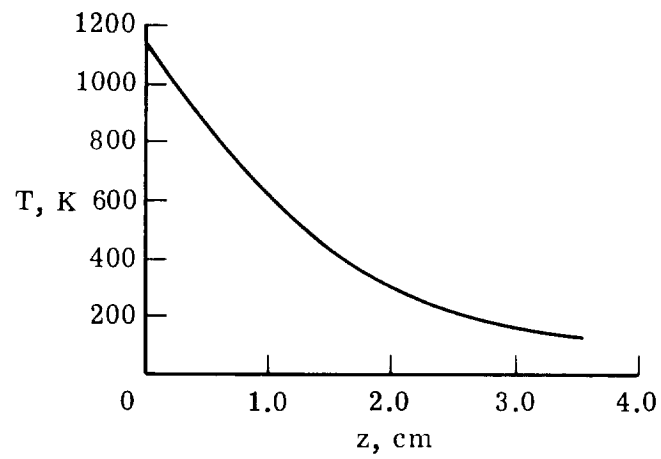
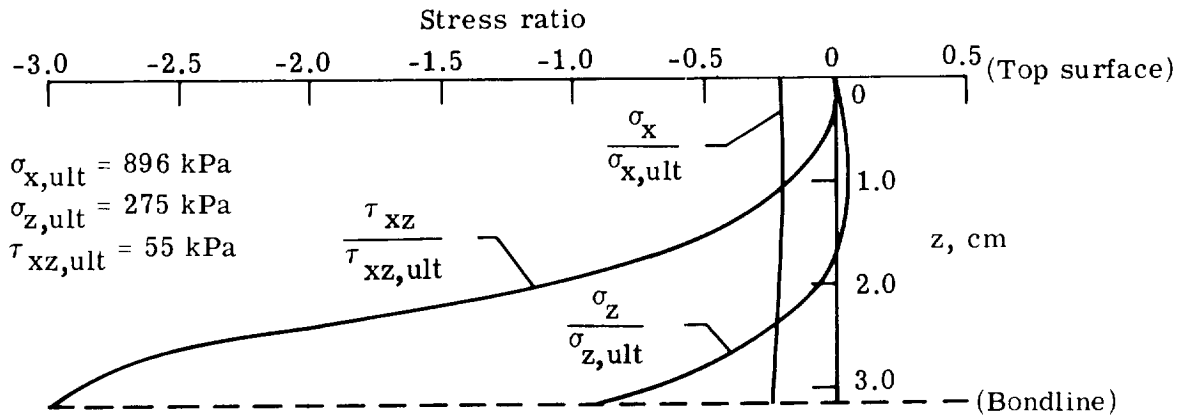Figure 34.- Maximum stress assuming extreme temperature conditions.
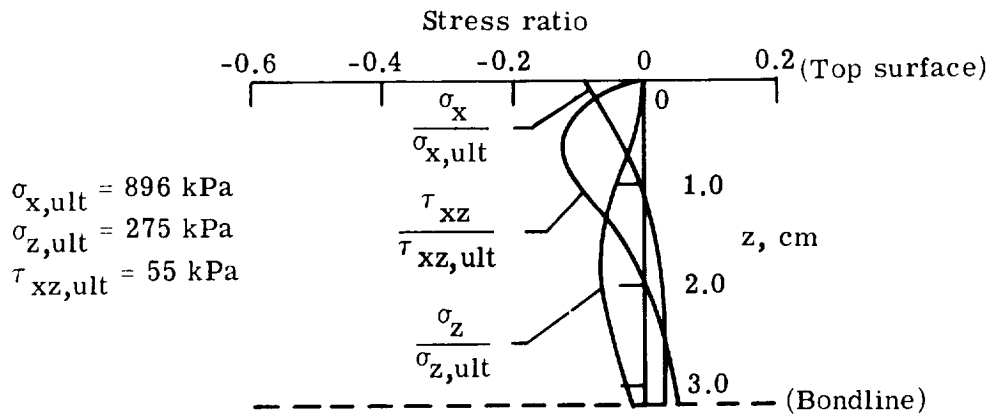
(a) Surface temperature history.

(b) Temperature gradient at t = 480 sec.

Figure 35.- Typical shuttle entry temperatures.

Stress ratio

(a) 160 K cold soak $\left(T_O = 295 \text{ K}\right)$.

Stress ratio

(b) 1144 K to 160 K gradient $\left(T_O = 160 \text{ K}\right)$.

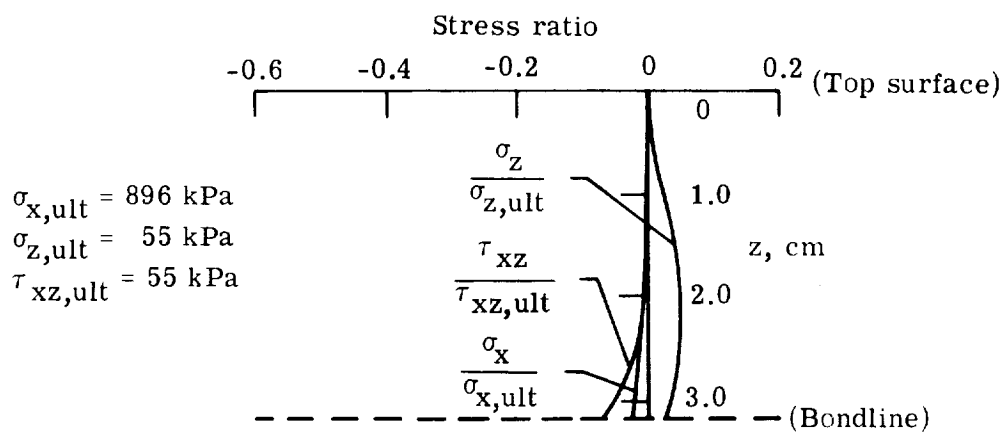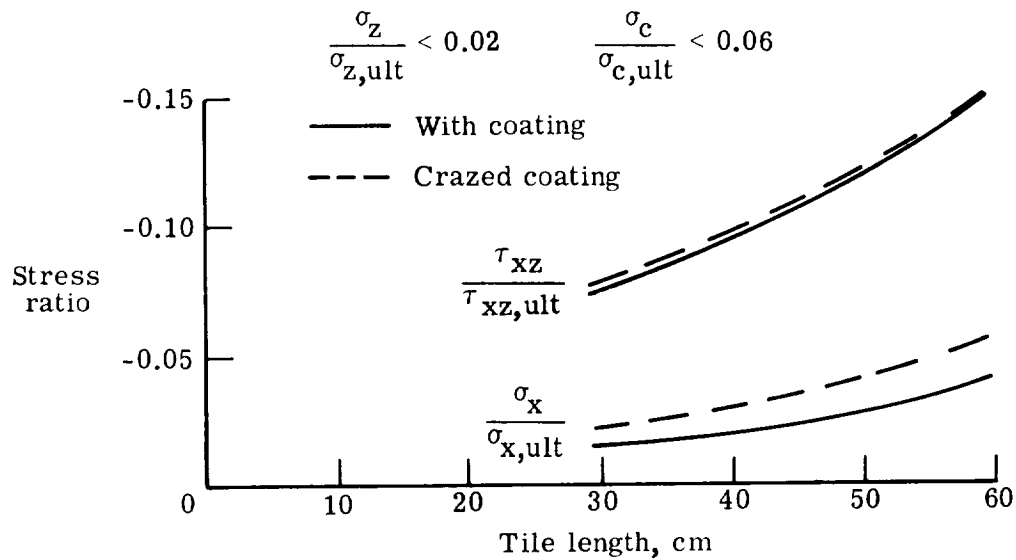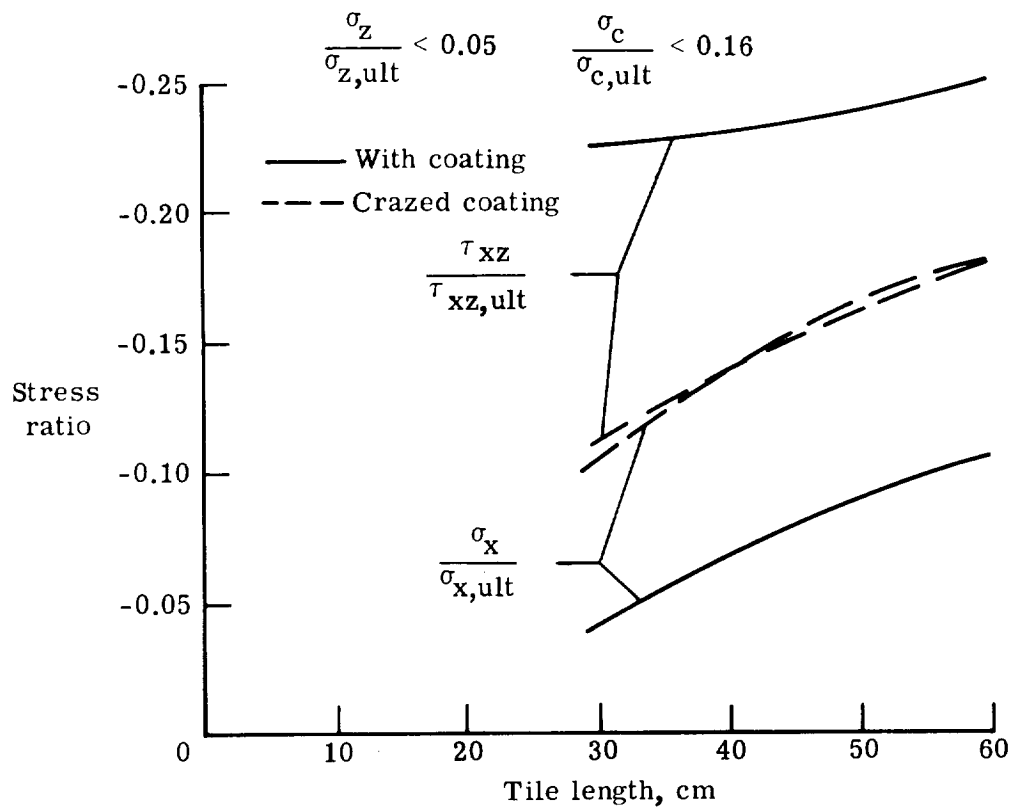Figure 36.- Maximum RSI stress with RTV-560 strain isolator, coating neglected.

Stress ratio

$\sigma_{x,ult}$ = 896 kPa
$\sigma_{z,ult}$ = 55 kPa
$\tau_{xz,ult}$ = 55 kPa

$\dfrac{\sigma_z}{\sigma_{z,ult}}$

$\dfrac{\tau_{xz}}{\tau_{xz,ult}}$

$\dfrac{\sigma_x}{\sigma_{x,ult}}$

(Top surface)

z, cm

(Bondline)

Figure 37.- Maximum RSI stress for 160 K cold soak with Nomex strain isolator, neglecting coating $\left(T_O = 295 \text{ K}\right)$.

$$\frac{\sigma_z}{\sigma_{z,ult}} < 0.02 \qquad \frac{\sigma_c}{\sigma_{c,ult}} < 0.06$$

(a) 160 K soak $\left(T_O = 295\ K\right)$.

$$\frac{\sigma_z}{\sigma_{z,ult}} < 0.05 \qquad \frac{\sigma_c}{\sigma_{c,ult}} < 0.16$$

(b) 1144 K to 160 K gradient $\left(T_O = 295\ K\right)$.

Figure 38.- Variation of maximum RSI stress with tile size.